



HAL
open science

A comprehensive numerical model for the pyrolysis of intumescent polymers: application to EVA-ATH compounds

Jianwei Shi, Germain Boyer, Valeri V. Mourzenko, Jean-François Thovert

► **To cite this version:**

Jianwei Shi, Germain Boyer, Valeri V. Mourzenko, Jean-François Thovert. A comprehensive numerical model for the pyrolysis of intumescent polymers: application to EVA-ATH compounds. *Chemical Engineering Science*, 2023, 268, pp.118385. 10.1016/j.ces.2022.118385 . hal-04019845

HAL Id: hal-04019845

<https://hal.science/hal-04019845>

Submitted on 8 Mar 2023

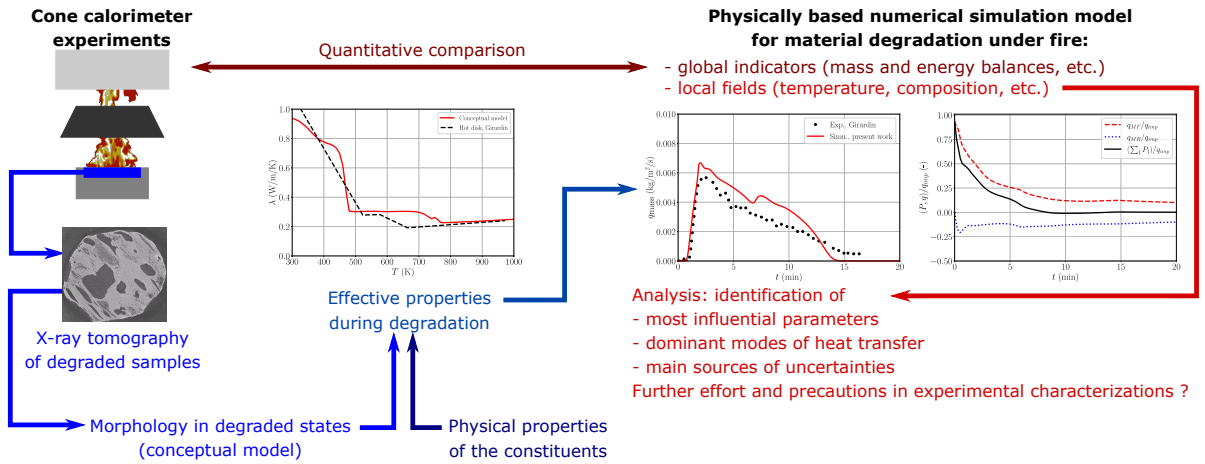
HAL is a multi-disciplinary open access archive for the deposit and dissemination of scientific research documents, whether they are published or not. The documents may come from teaching and research institutions in France or abroad, or from public or private research centers.

L'archive ouverte pluridisciplinaire **HAL**, est destinée au dépôt et à la diffusion de documents scientifiques de niveau recherche, publiés ou non, émanant des établissements d'enseignement et de recherche français ou étrangers, des laboratoires publics ou privés.

Graphical Abstract

A comprehensive numerical model for the pyrolysis of intumescent polymers: application to EVA-ATH compounds

Jianwei Shi, Germain Boyer, Valeri Mourzenko, Jean-François Thovert



Highlights

A comprehensive numerical model for the pyrolysis of intumescent polymers: application to EVA-ATH compounds

Jianwei Shi, Germain Boyer, Valeri Mourzenko, Jean-François Thovert

- The pyrolysis of ethylene-vinylacetate/alumina-trihydrate materials is studied.
- Models for thermal properties applicable along the material pyrolysis are proposed.
- Simulations of the material pyrolysis are compared to cone calorimeter experiments.
- The thermal balance of the material pyrolysis is analysed.
- The most influential phenomena on the material degradation process are identified.

A comprehensive numerical model for the pyrolysis of intumescent polymers: application to EVA-ATH compounds

Jianwei Shi^{a,b,1}, Germain Boyer^{b,*}, Valeri Mourzenko^a and Jean-François Thovert^a

^aInstitut P', CNRS - Université de Poitiers - ISAE-ENSMA, 11 bd Marie et Pierre Curie, TSA 41123, Poitiers CEDEX 9, 86073, France

^bInstitut de Radioprotection et de Sécurité Nucléaire (IRSN), PSN-RES/SA2I/LIE, , Cadarache, St Paul Lez Durance, 13115, France

ARTICLE INFO

Keywords:

Polymer composite
Porous residual
Effective properties
Pyrolysis modeling
Numerical simulation
Thermal balance

Abstract

A detailed numerical pyrolysis model is presented for the thermal degradation of ethylene-vinylacetate copolymers filled with alumina-trihydrate (EVA-ATH). The formulation involves effective thermal parameters and surface radiative emissivity that continuously follow the material evolution, deduced from its evolving morphology along the degradation, as characterized and modelled based on microtomographic imaging. The comparison of simulated and actual cone calorimeter experiments suggests that the ATH dehydration occurs on a broader range of temperature than generally assumed. The analysis of the thermal balance during the material degradation shows that only 40% of the incident flux is absorbed by the material due to the radiative behaviour of alumina, 13% is released at the backface, and the ATH dehydration represents 70% of the pyrolysis endothermicity. These results confirm the importance of the front- and back-face boundary conditions in reference experiments, and the need of an improved modelling of the ATH chemical degradation scheme and kinetics.

1. Introduction

The spread of electric cable fire is a major risk in nuclear safety, and for this reason, the French Institute for Radioprotection Nuclear Safety (IRSN) has carried out in recent years cable tray fire tests (Zavaleta and Audouin, 2017; Zavaleta et al., 2019) in the framework of the OECD PRISME 2 project in order to enhance the NRC CHRISTIFIRE database (Mc Grattan et al., 2010). This experimental approach aimed at providing engineering models capable to evaluate the global mass loss and heat release during a cable fire scenario as a function of the macroscopic properties of the cable configuration (number of trays, loading, spacing, type of cables, etc.).

A complementary approach to model cable fires may consist in directly predicting the materials degradation rate using autonomous comprehensive pyrolysis models. Some of them have recently been used to simulate the pyrolysis of cable sheaths or similar materials: in-house models developed on multiphysics packages (e.g. using Comsol (Witkowski et al., 2015; Girardin et al., 2015; Girardin, 2016; Bhargava et al., 2019)), pyrolysis softwares such as Thermakin (Stoliarov et al., 2010; Witkowski et al., 2015; Leventon et al., 2015; Swann et al., 2019), or similar models directly integrated in computational fire dynamics softwares such as FDS (Matala and Hostikka, 2011; Matala et al., 2012) or the CALIF³S-Isis software developed at IRSN (Boyer, 2017; Shi et al., 2018; Shi, 2019). All these models are based on the solution of conservation equations for the mass of condensed materials,

*Corresponding author

 germain.boyer@irsn.fr (G. Boyer)

ORCID(s):

¹Present address: School of Mechanical and Power Engineering, Zhengzhou University, 100 Science Avenue, Zhengzhou, 450001, China

the mass of pyrolysis volatiles and the total enthalpy of the two-phase system. Due to the complex and evolutive composition of the considered materials, these models are written for multi-component systems. However, even if the materials used in cable manufacturing generally produce porous and possibly intumescent residuals, their morphology is rarely accounted for with precision, and the conservation equations are rather solved for at the Darcy scale using homogenised quantities. This implies that effective properties involved in these conservation equations must be characterized or modelled, namely the permeability in the Darcy law for momentum conservation, the effective diffusivity in the Fick law in the gas species transport equations, the effective conductivity in the Fourier law for heat transfer, but also the effective surface emissivity and in-depth radiative properties when the radiative transfer equation is solved for. Yet, contrary to homogeneous, non-charring materials such as PMMA as an emblematic example (Stoliarov et al., 2009b; Bal and Rein, 2015), cable sheaths materials produce residuals during their pyrolysis whose morphological and thermal properties are hardly characterized. Two types of cables are commonly found in nuclear facilities (Zavaleta et al., 2013; Zavaleta and Audouin, 2017; Meinier et al., 2017): PVC-based halogenated electric cables, that produce highly intumescent residuals, and halogen-free electric cables made of a polyethylene-vinylacetate (abbreviated as EVA) matrix containing an alumina-trihydrate (ATH) grain load. In this second case, the final alumina residuals are porous and highly friable, which precludes their handling in the purpose of conductivity or specific heat milligram-scale characterizations.

That is why, in the particular case of EVA-ATH compounds, a complementary approach to the usual set of characterizations (Witkowski et al., 2012; Hoffendahl et al., 2015; Witkowski et al., 2015; Girardin et al., 2015) has been proposed to overcome this problem (Shi, 2019; Shi et al., 2020). It consists in predicting the material effective properties all along its degradation according to an evolutive conceptual model for its morphology and the local properties of the material components. In this work, the material morphology has been analysed based on to SEM and X-ray microtomography visualisations of the material pre-degraded at relevant degradation stages. In this manner, the effective properties can be analytically or semi-analytically expressed as functions of the component properties, characteristic quantities (scale-separated porosities, pores scales or aspect ratios, etc.) of the material morphology and local physical properties. This approach has been successfully applied to the prediction of the EVA-ATH effective conductivity (Shi et al., 2020).

The present article describes the principles of the pyrolysis numerical model developed for CALIF³S-Isis and its implementation for EVA-ATH compounds, which makes use of these earlier results. The main original features are the careful modelling of some of the material properties during its degradation, such as its effective thermal conductivity and its effective surface emissivity, based on a thorough preliminary analysis of the material morphology at a few successive stages, on a reasoned conceptual model for its evolution all along the process, and on the upscaling of the transport coefficients by use of theoretical arguments applied successively on the various scales of the multiscale

geometry. As well, contrary to FDS or Thermakin, the model describes the gaseous species transport by barycentric diffusion relative to a mean flow governed by Darcy's law, which also contributes in the energy balance equation. Applications are presented, which simulate the EVA-ATH degradation in the conditions of various cone calorimeter experiments (Girardin et al., 2015; Girardin, 2016; Sonnier et al., 2016).

The evolution of the material composition and morphology is presented in section 2. The pyrolysis module of the CALIF³S-Isis model, already used in previous works (Boyer, 2017; Shi et al., 2018) and adapted here for simulations with intumescent material, is presented in section 3. The models for the physical and effective properties involved in the pyrolysis model are described in section 4. Finally, section 5 compares quantitatively the results of simulations to those of cone calorimeter experiments of the literature (Girardin et al., 2015; Girardin, 2016; Sonnier et al., 2016) under similar operating conditions. A measure of the experimental uncertainties is proposed and compared to the discrepancies between the experimental and numerical data. Possible explanations for the observed differences are discussed. A global thermal balance is also depicted in order to identify the dominant heat transfer mechanisms, and subsequently the most sensible material properties.

2. Material description

2.1. Material composition and components degradation steps

The materials considered in the present work are EVA-ATH compounds made of Alumina trihydrate grains (ATH) embedded in an ethylene-vinylacetate copolymer matrix (EVA). The mass fraction of ATH in the material in its initial state M_0 is denoted by $Y_{ATH||M_0}$. During the degradation process, ATH undergoes a dehydration which converts it into alumina and releases water vapour. Dehydration occurs between 550 and 610 K according to thermogravimetric analyses carried out either for pure ATH (Laoutid et al., 2017; Redaoui et al., 2016; Strekopytov and Exley, 2006) or for EVA-ATH compounds (Hoffendahl et al., 2015; Witkowski et al., 2015; Girardin et al., 2015; Sonnier et al., 2016; Meinier et al., 2017). However, although it occurs mostly in this range, up to 20% of the water is possibly released at higher temperatures (Zivkovic and Dobovisek, 1977; Rivas Mercury et al., 2006; Zhu et al., 2010). The EVA decomposition depends on the initial mass content $Y_{VA||EVA,M_0}$ of vinylacetate (VA) in EVA. It involves two main steps. The first step is deacetylation which releases mainly acetic acid, although the presence of the ATH grains is supposed to induce a subsequent catalytic conversion of acetic acid into acetone, CO₂ and H₂O (Witkowski et al., 2015). Deacetylation generally occurs between 610 and 650 K. However, this step is generally either neglected or lumped with the ATH dehydration in the study of EVA-ATH compounds (Witkowski et al., 2015; Girardin et al., 2015), since the VA mass content in EVA is generally small (< 30%) and therefore, the mass and thermal signatures of the EVA deacetylation in milligram scale characterisations cannot be easily distinguished from the contribution of ATH dehydration. In a second step, the polyene chains resulting from the EVA deacetylation fully degrade between

750 and 800 K (Marcilla and Beltrán, 1995; Soudais et al., 2007; Hoffendahl et al., 2015; Witkowski et al., 2015; Girardin et al., 2015; Sonnier et al., 2016), with no solid residual, similarly to pure polyethylene (Stoliarov et al., 2009b; Kumar and Singh, 2013; Coelho et al., 2010; Agarwal and Lattimer, 2012). The released gases commonly observed in FTIR analyses coupled to TGA experiments on EVA are alkanes such as methane CH_4 and propane C_3H_8 , alkenes such as ethylene C_2H_4 (Witkowski, 2012; Girardin et al., 2015), but also α -dienes and aromatics compounds (e.g. benzene C_6H_6) (Witkowski, 2012). For later use, the gaseous species will be denoted as follows: water vapour as G_1 , carbon dioxide as G_2 , acetic acid as G_3 and acetone as G_4 (deacetylation products) and methane as G_5 , propane as G_6 , ethylene as G_7 and benzene as G_8 (final EVA decomposition products).

In the present work, cone calorimeter experiments carried out on self-made EVA-ATH compounds will be considered (Girardin et al., 2015; Girardin, 2016; Sonnier et al., 2016). These materials contain an ATH grain load $Y_{\text{ATH}||M_0} = 65\%$ (Girardin et al., 2015; Girardin, 2016) or 60% (Sonnier et al., 2016) in an EVA matrix with $Y_{\text{VA}||\text{EVA},M_0} = 28\%$. Their composition is similar to that of the samples of commercial electrical cable sheaths considered for morphological characterizations in previous works (Shi, 2019; Shi et al., 2020). For the sake of simplicity, values of $Y_{\text{ATH}||M_0} = 60\%$ and $Y_{\text{VA}||\text{EVA},M_0} = 28\%$ will be considered in the whole paper.

2.2. Material morphology according to SEM and X-ray tomography visualizations

Three states of the material were considered in a previous works (Shi, 2019; Shi et al., 2020) for morphological analysis: the virgin material, the state after fully completed ATH dehydration, and the final state after full EVA decomposition. These states were analysed using 2D SEM visualizations, which did not reveal any significant change of the volume of the $2\mu\text{m}$ mineral grains, even during the ATH dehydration. However, complex multiscale porous structures can be observed after ATH dehydration and EVA decomposition. Corresponding samples were prepared by cutting pieces from flattened cable sheaths to be placed in a cylindrical crucible and pre-degraded in an oven. They were analysed using X-ray tomography imaging with effective resolution of $10\mu\text{m}$. Only the main features are recalled here, the fully detailed description of the geometrical characterization and modelling can be found by Shi et al., 2020. The post-dehydration sample exhibited a total volume expansion along the direction of the cylinder axis corresponding to an intumescence factor $\beta = 1.4$. Then, the analysis of both degraded samples revealed four scales of porosity. The larger one is constituted of oblate ellipsoidal macropores with typical semi-axes $A \times \eta A \times \eta A$. After dehydration and final decomposition, A and η were evaluated to $70\mu\text{m}$ and $47\mu\text{m}$, and to 5.5 and 2.9, respectively. Spherical mesopores of average radius $R = 30\mu\text{m}$ were also observed at both degradation stages. This is consistent with a mechanical argument whereby the surface tension effects widely dominate the viscous shear stresses for bubbles with sizes in the range of the mesoporosity or smaller [47]. Furthermore, owing to mass and volume balance considerations and to the measured intumescence, the apparent solid observed in the tomographies necessarily contains micropores smaller than

the spatial resolution. These micropores were also assumed to be spherical. Finally, based on similar volume balance arguments, the $2\mu\text{m}$ ATH grains were assumed to become nanoporous during their dehydration. The values of the macroporosity Φ_{MP} , mesoporosity Φ_{mP} , microporosity $\Phi_{\mu P}$ and nanoporosity Φ_{vP} after ATH dehydration and EVA decomposition are reported in Figure 1.

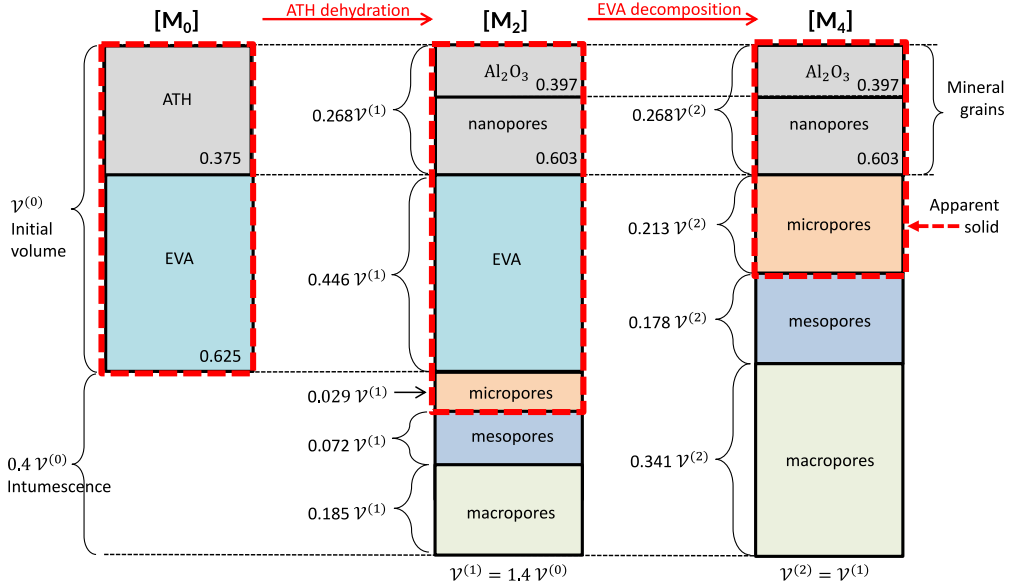


Figure 1: Volume fractions of voids and substances in the observed stages of degradation of EVA-ATH compounds.

2.3. Scenario for the material evolution

A comprehensive scenario for the morphological evolution of the material during its pyrolysis has been proposed, based on the observations from the tomographic images after complete ATH dehydration and EVA decomposition, and on reasoned physical arguments. Again, only the main features are recalled here, full details can be found in (Shi, 2019; Shi et al., 2020). In order to describe this scenario, two representations of the material degradation are proposed according to the two-component chemical composition of the material depicted in section 2.1, and to the evolution of the material morphology depicted in section 2.2. On the one hand, two independent progress variables associated with the ATH dehydration and EVA decomposition are defined based on the initial and current masses $m_{\text{ATH}}|_{M_0}$, m_{ATH} , $m_{\text{EVA}}|_{M_0}$ and m_{EVA} of ATH and EVA,

$$\alpha_{\text{ATH}} = 1 - m_{\text{ATH}}/m_{\text{ATH}}|_{M_0} \quad (1)$$

$$\alpha_{\text{EVA}} = 1 - m_{\text{EVA}}/m_{\text{EVA}}|_{M_0} \quad (2)$$

On the other hand, labels M_m are introduced to denote successive particular stages in the degradation process: onset (M_0); dehydration of ATH sufficient to provide the gas needed for the full development of the intumescence (M_1); complete dehydration of ATH (M_2); complete deacetylation (M_3); and ultimate stage of the degradation (M_4). By metonymy, M_m is also used to denote the state (compositional and morphological) of the degraded material at the corresponding stage. Furthermore, M_m can be used to denote a chemical pseudo-species, which includes all the condensed species present in the corresponding state (but excludes the gases). Note that in a reaction such as (6) which converts pseudo-species M_m into M_{m+1} , morphological changes (including pore volume fractions, shape factors and intumescence) are consubstantial with the compositional changes, as per the definition of the states M_m and M_{m+1} . A few intermediate stages/states ($M_{34\ddagger}$ and $M_{34\ddagger}$) are also introduced, but they only correspond to topological transitions, without associated pseudo-species. A graphic summary of the whole scenario is given in Figure 2, showing the evolutions of the main geometric parameters as functions of the two progress variables.

The modelling of the dehydration step rests on the following ideas. In view of the viscosity of the molten EVA, the rise of small gas bubbles is very slow (less than $0.5 \mu\text{m/s}$ for a diameter up to $200 \mu\text{m}$ (Shi, 2019)). Thus, during a first period, steam is confined in the sample which causes the intumescence and the development of the multiscale pore system. Since large bubbles necessarily result from the growth or coalescence of smaller ones, we consider in a schematized vision that the micro, meso and macroporosity develop sequentially, each of them up to the volume fractions measured in the post-dehydration tomography. The advancement α_{ATH} when the produced amount of steam, reaches the volume required for the constitution of each successive kind of porosity is easily determined from volume balance considerations. For instance, the state M_1 with micro, meso and macropores of volume fractions $\Phi_{\mu P, M_1} = 0.029$, $\Phi_{mP, M_1} = 0.072$ and $\Phi_{MP, M_1} = 0.185$ is reached when $\alpha_{\text{ATH}} = \alpha_{\text{ATH}, M_1}$ (Shi et al., 2020) which appears in Table 1.

From then on, a connected path to the outside exists. The gases subsequently produced are evacuated, the development of the pore system and the intumescence stop, and the pore fractions $\Phi_{\mu P}$, Φ_{mP} and Φ_{MP} remain constant, until stage M_2 where dehydration is complete, $\alpha_{A, M_2} = 1$. The nanopores occupy then 60.3% of the grains volume, i.e. $\Phi_{vP, M_2} = 0.162$.

During the two subsequent steps of the decomposition of the EVA matrix, the nanoporosity is unchanged but the EVA volume decreases and the micro-, meso- and macroporosity increase again. Similarly to the build-up of the initial cascade of porosities, we consider that the increments of the micro-, meso- and macroporosity occur sequentially. At the intermediate stage M_3 corresponding to the completion of the deacetylation (α_{EVA, M_3}) only the microporosity has increased, up to $\Phi_{\mu P, M_3} = 0.116$. Then, during the remaining EVA degradation, the microporosity increases further, and then the meso- and macroporosity, until they all reach final values $\Phi_{\mu P, M_4} = 0.213$ (at $\alpha_{EVA, \mu P}$), $\Phi_{mP, M_4} = 0.178$ (at $\alpha_{EVA, mP}$) and $\Phi_{MP, M_4} = 0.341$ (at $\alpha_{EVA, MP} = \alpha_{EVA, M_4} = 1$).

Table 1

Values of the progress variables associated with the pseudo-materials and the thresholds of formation of the porosity scales.

	M_1	M_2	M_3	$M_{34\dagger}$	$M_{34\ddagger}$	M_4	μP	mP	MP
α_{ATH}	5.14×10^{-4}	1	1	1	1	1	5.23×10^{-5}	1.82×10^{-4}	5.14×10^{-4}
α_{EVA}	0	0	0.195	0.522	0.769	1	0.413	0.652	1

Aside from the volume fractions of the various kinds of pores and condensed constituents, the modelling of the thermal conductivity in section 4.3.2 makes use of other features such as the pores sizes, shapes and aspect ratios (addressed in section 2.2), but also of the connectivities of various elements. Some of them never change. For instance in the grains, the nanoporosity is necessarily connected since a path must exist for the steam to leave the grain, and the solid phase must also be continuous since the grain are known to be cohesive from the start up to the very final state. But others undergo transitions during the degradation process, which requires to introduce a few additional threshold values of the progress variables.

The micropores are initially very sparse and regarded as unconnected inclusions, but as their volume fraction increases while the amount of EVA decreases, they eventually become connected. We assume that the transition takes place when the volume fraction $\Phi_{\mu P}$ of micropores exceeds that of the embedding polymer matrix X_{EVA} . This choice is partly arbitrary, but it has been checked that the precise value of the threshold has little influence on the results. The corresponding intermediate stage is denoted as $M_{34\dagger}$, at $\alpha_{EVA, M_{34\dagger}}$.

Similarly, the mineral grains are initially unconnected inclusions in the polymer matrix, but since the material remains mechanically stable (though friable) in the final degradation state, the grains necessarily become connected at some point during the EVA decomposition. Again, the threshold is chosen partly arbitrarily but without significant impact on the result, at mid-distance between the intermediate and final values of the grain volume fraction in the apparent solid. The corresponding degradation state, denoted as $M_{34\ddagger}$, is reached at $\alpha_{EVA, M_{34\ddagger}}$.

3. Pyrolysis modelling

The pyrolysis model depicted below is an improved version of the model used in previous works (Boyer, 2017; Shi et al., 2018) and is part of the CALIF³S-Isis fire simulation software developed at IRSN (Babik, 2021a,b). The mass and heat balance equations are formulated on the so-called Darcy scale, *i.e.*, in terms of local averages of the state variables, and involving effective transport coefficients whose modelling is presented in section 4.3.2. The heat and gas mass transfers are modeled under the hypothesis of local thermal and compositional equilibrium. This model is restricted to a monodimensional modelling, assuming that the heat and mass transfers are dominant in a given direction and negligible in the transverse ones. In what follows, x denotes the in-depth material coordinate, δ_M the

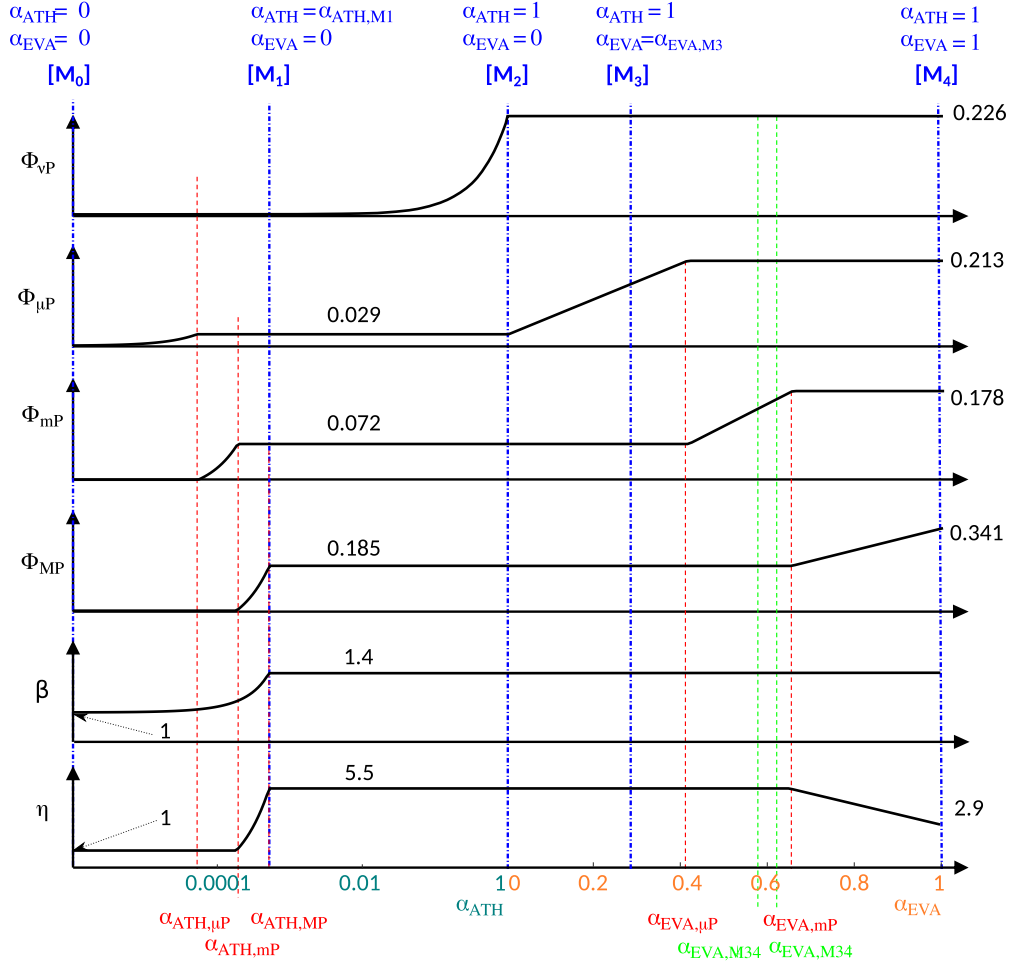


Figure 2: Evolution of the nanoporosity Φ_{vP} , microporosity $\Phi_{\mu P}$, mesoporosity Φ_{mP} , macroporosity Φ_{MP} , intumescence β and ellipsoid macropores aspect ratio η , as functions of the progress variables α_{ATH} (in logarithmic scale) and α_{EVA} (in linear scale).

sample thickness; $x = 0$ denotes the initial position of the irradiated face, and $x = \delta_M$ corresponds to the back face.

Volume variations are accounted for using an Arbitrary Lagrangian Eulerian (ALE) technique.

3.1. Degradation scheme

Accounting for the definition of the pseudo-species M_m and denoting by G_k the various pyrolytic gases introduced in section 2, one considers N_R sequential degradation reactions \mathcal{R}_i for the successive pseudo-species M_{i-1} , expressed in the following form (3):



where v_{ik} are the mass stoichiometric coefficients for gas production, and μ_i are the mass yields of the subsequent solid degradation states. Each degradation reaction is associated with an effective reaction rate denoted as $\tilde{\omega}_i$.

3.2. Conservation laws and boundary conditions

3.2.1. Mass conservation of the condensed pseudo-species

In a given volume, several condensed pseudo-species of apparent density ρ_{M_m} can occur with a volume fraction denoted as X_{M_m} , with

$$\sum_{m=1}^{N_M} X_{M_m} = 1 \quad (4)$$

Thus, let

$$\widetilde{\rho_{M_m}} = X_{M_m} \rho_{M_m} \quad (5)$$

denote the partial density of the pseudo-species (mass of M_m divided by the volume V containing the condensed substances and the pores). The conservation equations for the mass of each M_m are expressed as follows:

$$\partial_t \widetilde{\rho_{M_m}} + \partial_x \left(\widetilde{\rho_{M_m}} \overline{u_M} \right) = \mu_m \tilde{\omega}_m - \tilde{\omega}_{m+1} \quad (6)$$

where $\overline{u_M}$ is the solid phase deformation velocity resulting from the material shrinking or intumescence. Using the constraint (4), the set of equations (6) can be closed to determine $\overline{u_M}$. Note that the volume fractions also allow deducing the total porosity of the material from the porosity Φ_{M_m} of each material degradation state:

$$\Phi = \sum_{m=1}^{N_M} X_{M_m} \Phi_{M_m} \quad (7)$$

3.2.2. Gaseous species mass and momentum conservation

Since the gas mass is not accounted for in the previous balance, transport equations, including diffusion and convection, for the N_G gaseous species G_k are also solved for:

$$\partial_t \left(\overline{\rho_G Y_{G_k}} \right) + \partial_x \left(\overline{\rho_G Y_{G_k}} \overline{u_G} \right) = \partial_x \left(\overline{\rho_G} D_{Y,\text{eff}} \partial_x \overline{Y_{G_k}} \right) + \sum_{i=1}^{N_R} v_{ik} \tilde{\omega}_i \quad (8)$$

Here, $\overline{\rho_G}$, $\overline{Y_{G_k}}$ and $\overline{u_G}$ are the intrinsic gas phase average density, species mass fractions and velocity, and $D_{Y,\text{eff}}$ is the effective diffusivity. If W_{G_k} denotes the gaseous species molar masses, $\overline{\rho_G}$ is determined by the perfect gas law

assuming that the pressure variations $\overline{p_G'} = \overline{p_G} - p_0$ around the atmospheric pressure p_0 are small:

$$p_0 = \frac{\overline{\rho_G R T}}{W_G} \quad \text{with} \quad \frac{1}{W_G} = \sum_{k=1}^{N_G} \frac{\overline{Y_{G_k}}}{W_{G_k}} \quad (9)$$

The intrinsic gas phase average velocity is obtained by solving the Darcy law:

$$\Phi(\overline{u_G} - \overline{u_M}) + \frac{K}{\mu_G} (\nabla \overline{p_G'}) = 0 \quad (10)$$

Here, K is the permeability and μ_G is the gas viscosity. In this formulation, the material deformation is accounted for, but the gravity is supposed to be negligible compared to the viscosity effects. Note that Darcy's law (10) is applicable without correction for inertial effects. An upper bound of the pore scale Reynolds number $Re \approx 0.12$ can be estimated a priori based on the macropores scale $l = A < 100 \mu\text{m}$ (section 2.2), on a typical value of the maximal mass loss rate per unit area measured in the cone calorimeter experiments $q_{\text{mass,max}} < 0.01 \text{ kg/m}^2/\text{s}$ (Figs. 4, 5 and 6) and on the dynamic viscosity $\mu \approx 3 \times 10^{-5} \text{ kg/m/s}$ of water vapour at 800 K (species most likely to be released at the peak mass loss rate).

3.2.3. Enthalpy conservation

The enthalpy conservation equation is obtained by a volume average of the multicomponent formulation of Kuo, 1986. It is written in sensible enthalpy formulation. The sensible enthalpy laws for the condensed and gaseous species are :

$$h_{M_m}^s(T) = \int_{T_{\text{ref}}}^T c_{p,M_m}(\theta) d\theta \quad h_{G_k}^s(T) = \int_{T_{\text{ref}}}^T c_{p,G_k}(\theta) d\theta \quad (11)$$

where c_{p,M_m} and c_{p,G_k} are the specific heat capacities of the condensed and gaseous phases. In what follows, $\overline{h_{M_m}^s}$ and $\overline{h_G^s}$ denote the values of the sensible enthalpies expressed at the intrinsic average temperature \overline{T} , and $\Delta h_{\mathcal{R}_i}$ denote the heat of pyrolysis associated with reaction \mathcal{R}_i . Thus, the sensible enthalpy conservation equation, including diffusive, convective and radiative transfers, reads:

$$\begin{aligned} \partial_t \left(\sum_{m=1}^{N_M} \overline{\rho_{M_m}} \overline{h_{M_m}^s} + \Phi \overline{\rho_G} \overline{h_G^s} \right) + \partial_x \left(\sum_{m=1}^{N_M} \overline{\rho_{M_m}} \overline{h_{M_m}^s} \overline{u_M} + \Phi \overline{\rho_G} \overline{h_G^s} \overline{u_G} \right) = \\ - \sum_{i=1}^{N_R} \Delta h_{\mathcal{R}_i} \tilde{\omega}_i - (\partial_t \overline{p_G} + \overline{u_G} \partial_x \overline{p_G}) + \partial_x \left(\lambda_{\text{eff}} \partial_x \overline{T} \right) - \partial_x \overline{q_{\text{rad}}} \quad (12) \end{aligned}$$

Here, λ_{eff} denotes the effective conductivity, and $\widetilde{q}_{\text{rad}}$ is the volume averaged radiative heat flux travelling in the $x > 0$ direction. This flux is calculated by solving for the S2 non-symmetric approximation of the Radiative Transfer Equation (Modest, 2003). It can be decomposed into an upstream and a downstream component: $\widetilde{q}_{\text{rad}} = q_{\text{rad}}^+ - q_{\text{rad}}^-$. These two half fluxes verify the following ordinary differential equations:

$$\begin{cases} \partial_x q_{\text{rad}}^+ &= 2\kappa_{\text{eff}}(n_{\text{eff}}^2 \sigma \overline{T}^4 - q_{\text{rad}}^+), \\ -\partial_x q_{\text{rad}}^- &= 2\kappa_{\text{eff}}(n_{\text{eff}}^2 \sigma \overline{T}^4 - q_{\text{rad}}^-) \end{cases} \quad (13)$$

where κ_{eff} is the radiative absorption and n_{eff} is the effective refraction index.

3.2.4. Boundary condition at the irradiated face

At the irradiated side, the pyrolysis gases are ejected. The solid domain surface moves according to the swelling rate deduced from Equation (4). The hydrodynamic pressure is fixed to zero. The sum of the conductive, convective and radiative fluxes is continuous across the irradiated interface. However, the contribution of the heat convection by the exhausting gases is obviously continuous, as well as the radiative flux since semi-transparency is accounted for. As a consequence, the conductive flux on the material side is balanced by the diffusive and turbulent heat exchange at the vicinity of the sample surface. In actual fire simulations with the CALIF³S-Isis software, separate (coupled) solvers handle the regions within the degrading material and in the surrounding fluid phase. In the present case, the pyrolysis module is used as a stand-alone application, with a simplified representation of the surrounding fluid. Its temperature T_F is supposed to be uniform, and the heat exchange between the solid surface at temperature \overline{T}_{MF} and the surrounding fluid can be modeled by the means of a fixed heat exchange coefficient $h_{\text{exch},MF}$, so that

$$-\lambda_{\text{eff}} \partial_x \overline{T} = -h_{\text{exch},MF} (\overline{T}_{MF} - T_F) \quad (14)$$

For the radiative balance, two radiative sources can be considered: on the one hand, the heat flux q_{imp} imposed by an external source (typically a cone heater); and the radiative flux imposed by the presence of a flame q_{fl} . The radiative balance at the interface is accounted for by introducing the material transmissivity τ_{eff} in the present case of semi-transparent materials: the total incident radiative flux $q_{\text{inc}} = q_{\text{imp}} + q_{\text{fl}}$ is partly reflected ($q_{\text{rad,ref}} = (1 - \tau_{\text{eff}})q_{\text{inc}}$) and partly absorbed, whereas the material loses radiative power by in-depth emission ($q_{\text{rad,ref}} = \tau_{\text{eff}} q_{\text{rad}}^- / n_{\text{eff}}^2$). In these conditions, the net radiative flux $\widetilde{q}_{\text{rad}}$ at the sample surface in the $x > 0$ direction reads:

$$\widetilde{q}_{\text{rad}} = \tau_{\text{eff}} \left(\varphi_{\text{inc}} - \frac{q_{\text{rad}}^-}{n_{\text{eff}}^2} \right) \quad (15)$$

and the two half-fluxes on the material side verify the following boundary condition:

$$q_{\text{rad}}^+ = \tau_{\text{eff}} q_{\text{inc}} + \left(1 - \frac{\tau_{\text{eff}}}{n_{\text{eff}}^2} \right) q_{\text{rad}}^- \quad (16)$$

Note that the mass loss rate (MLR) of pyrolysis gases ejected at the exposed surface

$$q_{\text{mass}} = \overline{\rho}_G \Phi (\overline{u}_G - \overline{u}_M) \quad (17)$$

and the associated mass fractions \overline{Y}_{G_k} can be used to estimate the heat release rate (HRR) per unit area q_{comb} due to the complete combustion of these gases:

$$q_{\text{comb}} = \left(\sum_{k=1}^{N_G} \Delta h_{c,k} \overline{Y}_{G_k} \right) q_{\text{mass}} \quad (18)$$

Here, $\Delta h_{c,k}$ denote the heats of combustion of the gaseous species.

3.2.5. Backface boundary condition

At the backface, the material is supposed to be placed on an opaque insulating layer. The solid displacement is null and the pyrolysis gases mass flux is null (impervious condition), but the model can also accommodate mass losses if the gases are allowed to exude at the rear face, with associated convective heat losses. The backface heat flux is modelled assuming that the temperature is continuous, the insulator is opaque which implies a null radiative flux, and the boundary is impervious. The only remaining term is the conductive flux, so that:

$$-\lambda_{\text{eff}} \partial_x \overline{T} = -\lambda_B \partial_x T_B \quad (19)$$

Here T_B is the temperature within the insulator and λ_B is its conductivity; with ρ_B its density and $c_{p,B}$ its heat capacity. Heat transfer in this medium is modeled by a simple Fourier equation

$$\rho_B c_{p,B} \partial_t T_B - \partial_x (\lambda_B \partial_x T_B) = 0, \quad (20)$$

At the external side of the insulator, the heat exchange with the external domain at temperature T_E is accounted for by prescribing $-\lambda_B \partial_x T_B = h_{\text{exch},BE} (T_{BE} - T_E)$.

3.3. Numerical modelling

The conservation equations depicted above are discretised according to a finite volume formulation coupled with an ALE technique (Donea et al., 2004) to account for the 1D volume domain variations. This comes to introduce a moving grid of arbitrary displacement velocity u_d . The condensed mass conservation equation (6) coupled with the volume constraint (4) are solved in three steps: firstly, (6) is solved in Lagrangian formulation with first order backward Euler approximation of the time derivative to estimate the updated mass of the pseudo-materials encompassed in each cell; secondly, constraint (4) is used to assess the updated value of the sample thickness δ_M ; thirdly, the ALE grid is updated according to the new value of δ_M . The grid displacement follows the condensed phase displacement at the irradiated and the backface sides, and the grid cell sizes are homothetically adapted. This allows accounting for either surface regression or intumescence. Subsequently, this allows solving for the ALE formulation of the finite volume discretisation of conservation equations (8) and (12). The convective and diffusive terms are approximated by second order centred finite difference schemes, and the time stepping is carried out by a first order backward Euler approximation. Finally, the S2 approximation of the Radiative Transfer Equation (13) is solved for using a first order backward approximation of the fluxes derivatives.

In the simulations presented in this work, time step $\delta t = 1$ s and initial grid cell size $\delta x = 2 \times 10^{-5}$ m are used. These choices ensure converged results, in the sense of the characteristic times depicted in section 5.2, by less than 2.5% (see Appendix B).

4. Physical and effective properties

4.1. Material porosities and apparent densities

The apparent densities ρ_{M_m} of the materials M_m (excluding the negligible mass of gases encompassed in the pores contained in M_m) can be deduced from their composition presented in section 2.3 and from the densities of the constituents, $\rho_{\text{ATH}} = 2400$ kg/m³ (massive Gibbsite, Wefers and Misra, 1987), $\rho_{\text{AL}} = 3950$ kg/m³ (Auerkari, 1996) and $\rho_{\text{EVA}} = 950$ kg/m³ (Girardin, 2016). This yields $\rho_{M_0} = 1494$ kg/m³, $\rho_{M_1} = 1067$ kg/m³, $\rho_{M_2} = 843$ kg/m³, $\rho_{M_3} = 762$ kg/m³ and $\rho_{M_4} = 422$ kg/m³.

The total porosities of the various materials are the sums of their porosities on different scales as depicted in Figure 1,

$$\Phi_{M_m} = \Phi_{\nu P, M_m} + \Phi_{\mu P, M_m} + \Phi_{mP, M_m} + \Phi_{MP, M_m} \quad (21)$$

which yields $\Phi_{M_0} = 0$, $\Phi_{M_1} = 0.285$, $\Phi_{M_2} = 0.447$, $\Phi_{M_3} = 0.534$ and $\Phi_{M_4} = 0.893$.

4.2. Thermochemical properties

Considering the general shape of the degradation scheme (3) and the definition of the condensed pseudo-materials and the released gas species (sections 2.3 and 2.1), the actual degradation path is defined as follows: reaction \mathcal{R}_1 denotes the first step of intumescence formation due to the early release of water vapour, \mathcal{R}_2 corresponds to the main dehydration step, \mathcal{R}_3 corresponds to the EVA deacetylation and \mathcal{R}_4 corresponds to the final EVA decomposition. Recalling that the material composition is fully characterised by the ATH grain load ($Y_{GR}^{(0)} = 0.6$) and the VA content in EVA ($Y_{VA||EVA}^{(0)} = 0.28$), the mass stoichiometric coefficients associated with reactions of form (3) can be expressed as functions of these two parameters and of the molar masses of the condensed and gaseous substances involved in the degradation of EVA-ATH compounds. The numerical values of these coefficients are reported in Table 7, Appendix A.

Local thermal and compositional (for the gaseous species) equilibrium is assumed in the small averaging volumes over which the kinetic laws for the reactions are formulated. The effective reaction rate $\tilde{\omega}_i$ for reaction \mathcal{R}_i is expressed as an Arrhenius law,

$$\tilde{\omega}_i = A_{S,i} e^{\frac{-E_{a,i}}{RT}} \overline{\rho}_{M_{i-1}} \quad (22)$$

Here, $A_{S,i}$ is called pre-exponential factor (s^{-1}), $E_{a,i}$ is the activation energy (J/mol), $R = 8.314$ J/mol/K is the perfect gas constant, \overline{T} denotes the intrinsic volume average temperature (uniform over the averaging volume), and $\overline{\rho}_{M_{i-1}}$ is the volume average density of the chemical pseudo-species M_{i-1} .

The Arrhenius constants used in the present work are extracted from the characterizations of Girardin et al., 2015 and are adapted for the present degradation path. In particular, the Arrhenius constants for the EVA deacetylation is deduced from the isoconversional analysis presented in this reference. The heats of pyrolysis associated with reactions \mathcal{R}_1 and \mathcal{R}_2 are deduced from the values measured for pure ATH (Wefers and Misra, 1987; Hemingway et al., 1977). The heat of pyrolysis associated with EVA deacetylation \mathcal{R}_3 is deduced from these values and the value given by Girardin et al., 2015 for a reaction including ATH dehydration and EVA deacetylation. The heat of pyrolysis for reaction \mathcal{R}_4 coincides with the second reaction of Girardin et al., 2015. The Arrhenius constants and the heats of pyrolysis used in the present work are reported in Table 8, Appendix A.

The specific heat capacities of the pseudo-materials are deduced from values taken from the literature, expressed in the form $c_p = a + bT - c/T^2$. The coefficients a , b and c are reported in Table 9, Appendix A, for each material. The resulting specific heats for stages M_0 , M_2 and M_4 , in the range of temperature where they are expected to prevail, differ from the DSC measurements of Girardin et al., 2015; Girardin, 2016; Witkowski et al., 2015 by no more than 23 %, 16 % and less than 2 %, respectively. These differences do not exceed the measurement uncertainties reported by (Girardin, 2016).

In the gas phase, the temperature dependence of the specific heat capacities c_{p,G_k} are taken from Linstrom and Mallard, 2001. The evaluation of the total heat release rate (18) requires to provide the heats of combustion $\Delta h_{c,k}$ of the gaseous species involved in the material decomposition. Obviously, $\Delta h_{c,1} = \Delta h_{c,2} = 0$ J/kg (H₂O, CO₂); for the flammable gases, the values are extracted from Kanury, 1975 and are reported in Appendix A.

4.3. Effective transport coefficients

The homogenized balance equations formulated in section 3 involve several effective transport coefficients, such as the effective gas diffusivity $D_{Y,\text{eff}}$ in (8), the permeability K in (10), the effective conductivity Λ_{eff} in (12), the effective volume radiative coefficients κ_{eff} and n_{eff} occurring in (13) and the surface transmittivity τ_{eff} in (15). The following sections describe how they are modelled as functions of the state variables which characterize the current state of the material.

4.3.1. Effective transport properties for the gas phase

The effective diffusivity $D_{Y,\text{eff}}$ can be modelled as

$$D_{Y,\text{eff}} = C_D \Phi D_{\text{mol}} \quad (23)$$

where C_D is a calibrating constant allowing to switch between negligible ($C_D = 0$) to full ($C_D = 1$) species diffusion. Yet, according to Shi, 2019, the choice of C_D has a marginal influence on the results. For the sake of simplicity, the value $C_D = 1$ will be chosen.

The material permeability is evaluated by a mixing rule, based on the current composition and on the permeabilities K_{M_m} of the various degradation states M_m :

$$K = \sum_{m=1}^{N_M} X_{M_m} K_{M_m} \quad (24)$$

Rough estimates of the permeability at the post-dehydration ($K \approx 10^{-13}$ m²) and final decomposition states ($K \approx 10^{-11}$ m²) have been proposed in Shi, 2019 by the numerical simulation of the Stokes problem in the geometry extracted from the X-ray tomographies. These values are necessarily under-estimated since a non-negligible part of the total porosity was included in the apparent solid. However, sensitivity analyses have shown that, in this permeability range, the influence of permeability variations is negligible because the pressure increase resulting from the material degradation is by far smaller than the atmospheric pressure. These values have therefore been applied to the considered degradation states $K_{M_1} = K_{M_2} = K_{M_3} = 10^{-13}$ m² (post dehydration and deacetylation), and $K_{M_4} = 10^{-11}$ m² (final decomposition).

4.3.2. *Effective conductivity*

An evolutive conductivity model was devised and fully described in earlier works (Shi, 2019; Shi et al., 2020). Only its main features are recalled here. The model involves a four-stage upscaling procedure, for the nanoscale (grains), microscale (apparent solid), mesoscale and macroscale (observable in the tomographies). It relies on combinations of two classical models, namely the Differential Effective-Medium (DEM) model (Bruggeman, 1935) and the Symmetric Self-Consistent (SSC) scheme (Bruggeman, 1935; Landauer, 1952). The former is appropriate in situations where a composite features unconnected inclusions in a continuous matrix (e.g., ATH grains in the EVA matrix before $\alpha_{\text{EVA},M_{34\dagger}}$, or microporous apparent solid before $\alpha_{\text{EVA},M_{34\dagger}}$) while the latter is adequate for bicontinuous mixtures of two (or more) phases (e.g., nanoporous mineral grains, or microporous apparent solid beyond $\alpha_{\text{EVA},M_{34\dagger}}$).

Thus, the effective material conductivity Λ_{eff} can be expressed analytically in any instantaneous state of the system as a function of the current morphological features ($\Phi_{\nu P}$, $\Phi_{\mu P}$, Φ_{mP} , Φ_{MP} , X_{GR} , η and various connectivity criteria) supplemented by the conductivities of the constituents. The former are all expressed as analytic functions of the progress variables (1) and (2) in the framework of the evolutive geometrical model presented in section 2.2. The latter are functions of the current temperature, as described in figure 15, Appendix A.

Note that both DEM and SSC can be applied in anisotropic media, such as those resulting from the existence of the ellipsoidal acropores and yield in such situations a full, anisotropic conductivity tensor. However, the pyrolysis model is implemented in 1d, along the direction of the material degradation and intumescence, which corresponds to minor axis of the oblate ellipsoids. Therefore, the corresponding component λ_{eff} of the conductivity tensor is used in practice.

It has been shown that the results obtained with this method remarkably coincide with the effective conductivities calculated by direct numerical solution of the heat conduction problem in the geometries provided by the tomographies in the intermediate and final states of the actual material. They also agree within 10 % with the conductivities measured by Girardin, 2016 at ambient temperature for the virgin state M_0 , and for pre-degraded samples in states M_2 and M_4 in the range of temperature where they are expected to prevail. These discrepancies remain within the experimental uncertainty range of 20 % estimated by Girardin, 2016 for hot disk measurements.

4.3.3. *Radiative properties*

In the present work, material semi-transparency is accounted for and the effective absorption coefficient κ_{eff} , the surface transmissivity τ_{eff} and the refraction index n_{eff} must be modelled.

For material states M_0 , M_1 , M_2 and M_3 , the EVA matrix covers the ATH/alumina grains and the values measured by Girardin et al., 2015 for the virgin material can be used: $\kappa_{M_0} = \kappa_{M_1} = \kappa_{M_2} = \kappa_{M_3} = 8200 \text{ m}^{-1}$ and $\tau_{M_0} = \tau_{M_1} = \tau_{M_2} = \tau_{M_3} = 0.95$. These transmissivities are close to that found for polyethylenes ($\tau = 0.92$) (Stoliarov et al., 2009b,a). The refractive index is the one of polyethylene, $n_{M_0} = n_{M_1} = n_{M_2} = n_{M_3} = 1.5$ (Tsilingiris, 2003).

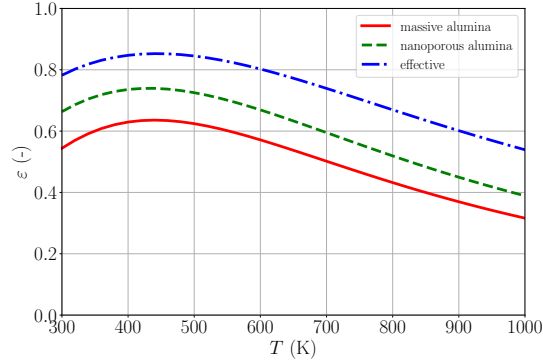


Figure 3: Temperature dependence of the spectrally integrated emissivity of massive alumina (Rozenbaum et al., 2009), and of the estimated emissivities of nanoporous alumina and of the EVA-ATH final residual.

For the final residual made of porous alumina, the in-depth radiative material behaviour is difficult to evaluate, so an arbitrary value $\kappa_{M_4} = 10^5 \text{ m}^{-1}$ has been chosen to impose an opaque behaviour, and the refraction index of the massive alumina is used ($n_{M_4} = 1.58$) (Sauerwein, 2014).

Based on this approximation, the surface transmissivity can be identified to the surface emissivity $\tau_{M_4} = \epsilon_{M_4}$ and be modelled using the effective emissivity formulation for a solid material with outcropping pores and the emissivity of massive alumina (Sih and Barlow, 2004) as follows (Shi, 2019). According to Bedford, 1988, the effective emissivity of a surface with pore surface fraction A_G is equal to $\epsilon = \epsilon_S(1 - A_G) + \epsilon_G A_G$, where ϵ_S and ϵ_G are the solid and gas surface emissivities. The latter is an apparent coefficient, which accounts for the emissivity of the solid surfaces of the outcropping pores. It can be approximated as $\epsilon_G = \epsilon_S / (\epsilon_S + f(1 - \epsilon_S))$, where $f = 1/6$ for cylindrical cavities with unit aspect ratio. The upscaled emissivity is obtained by a recursive application of this model. Starting from the spectral emissivity dependence (Rozenbaum et al., 2009) of alumina $\hat{\epsilon}_{AL}$, four upscalings are applied to account for the porosities on the various scales (Shi, 2019, sec9.1.3). For instance in the first one, ϵ_S is the emissivity $\hat{\epsilon}_{AL}$ of massive alumina and A_G is the pore volume fraction in the grains. It yields the grain emissivity $\hat{\epsilon}_{vAL}$, which plays the role of ϵ_S in the second upscaling while A_G is the pore volume fraction in the apparent solid. The mesoporosity and finally the macroporosity are treated in a similar way. Then, the spectral emissivity $\hat{\epsilon}_{M_4}$ can be convoluted with blackbody energy spectral densities at different temperatures to obtain the temperature dependence of the emissivity ϵ_{M_4} sought for. The temperature dependences of the massive alumina emissivity ϵ_{AL} , porous grain emissivity ϵ_{vAL} , and final state emissivity ϵ_{M_4} deduced from the 4 upscalings, are reported in figure 3.

When a mixture of pseudo-materials is present, a volume-weighted mixing rule similar to (24) is used for the evaluation of the effective radiative properties, namely in-depth absorption and refraction index, and surface transmissivity.

Table 2

Experimental conditions, measurements and material characteristics of the test cases considered for comparison with numerical simulations.

Case	[GIR_CAMLC_50_3]	[GIR_CONE_35_3]	[SON_CONE_35_4]
Atmosphere	inert	oxydative	oxydative
q_{imp} (kW/m ²)	50	35	35
q_{flame} (kW/m ²)	(-)	11	11
Mass loss rate	yes	yes	yes
Heat release rate	no	yes	yes
Backface temperature	yes	yes	no
t_{ig} (s)	(-)	65	90
δ_M (mm)	3	3.3	4
ρ_B (kg/m ³)	890	890	120
$c_{p,B}$ (J/kg/K)	1100	1100	1090
λ_B (W/m/K)	0.26	0.26	0.21

5. Results and discussion

5.1. Cone calorimeter experiments

Three cone calorimeter experiments are considered for quantitative comparison with numerical simulations. The first one, denoted as [GIR_CAMLC_50_3], has been carried out on $\delta_M = 3$ mm thick EVA-ATH samples by Girardin et al., 2015. The test was performed in inert atmosphere under an imposed cone flux q_{imp} of 50 kW/m². The second case [GIR_CONE_35_3] regards $\delta_M = 3.3$ mm thick slabs of the same material (according to mass loss measurements), but this time in open atmosphere under 35 kW/m² (Girardin, 2016). The third case [SON_CONE_35_4] has also been carried out in open atmosphere with 35 kW/m², but on $\delta_M = 4$ mm samples (Sonnier et al., 2016). Here, the additional thermal stress imposed by the flame in open atmosphere conditions is set to $q_{\text{fl}} = 11$ kW/m² according to usual rough estimates for pyrolysing polymers (Stoliarov et al., 2009b, 2010), and occurs after a fixed delay corresponding to the experimentally measured time-to-ignition t_{ig} . The samples lay on 50 mm thick insulators, whose thermal properties are reported in Table 2 along with the other parameters of the operating conditions. The external temperatures T_F and T_E used in the boundary conditions are set equal to a reference ambient temperature of 300 K.

5.2. Estimation of the experimental uncertainties

Several measurements are available for these tests: mass loss and mass loss rate, heat release rate, estimated by measurement of the oxydizer depletion and to be compared to the numerical estimation (18) and backface temperature (see Table 3). Several quantities are proposed to make quantitative comparisons: the times of peak mass loss rates (one $t_{\text{peak},1}$ for cases [GIR_CAMLC_50_3] and [GIR_CONE_35_3], two $t_{\text{peak},1}$ and $t_{\text{peak},2}$ for case [SON_CONE_35_4]); the characteristic times t_{25} , t_{50} and t_{75} required to reach 25%, 50% and 75% of the total

Table 3

Pyrolysis characteristic times (min) measured in the considered experiments.

Case	$t_{\text{peak},1}$	$t_{\text{peak},2}$	t_{25}	t_{50}	t_{75}	t_{ATH}	t_{VA}	t_{EVA}
[GIR_CAMLC_50_3]	2.67	(-)	4.52	9.18	18.85	4.02	6.17	(-)
[GIR_CONE_35_3]	2.52	(-)	3.36	6.90	13.04	4.67	6.45	9.27
[SON_CONE_35_4]	2.00	9.68	3.33	6.41	10.0	(-)	(-)	(-)

relative mass loss; and characteristic times t_{ATH} , t_{VA} and t_{EVA} associated with the completion of the different steps of the material degradation, defined as the times recorded when the backface temperature exceeds the characteristic temperatures of ATH dehydration (580 K), EVA deacetylation (650 K) and EVA final decomposition (750 K), which correspond to the pyrolysis phases when the corresponding degradation reaction is mostly completed. All these characteristic times are reported in Table 3.

It must first be noticed that, in spite of the similar thermal stress applied on the samples during all these tests, large experimental discrepancies arise in the mass loss measurements. In this respect, for Girardin's experiments, the pyrolysis process lasts noticeably longer in case [GIR_CAMLC_50_3] than in case [GIR_CONE_35_3]. This suggests that the total incident flux can be expected to be similar or even lower, in case [GIR_CONE_35_3], and that the choice of $q_{\text{flame}} = 11 \text{ kW/m}^2$ is physically relevant. However, this faster pyrolysis in case [GIR_CONE_35_3] is surprisingly associated with slightly longer times for ATH dehydration and EVA decomposition compared to case [GIR_CAMLC_50_3]. Surprisingly also, test case [SON_CONE_35_4], though carried out with a thicker sample, exhibits a shorter pyrolysis duration compared to case [GIR_CONE_35_3]. This might be because the rockwool used as an insulating material in case [SON_CONE_35_4] has a smaller effusivity $\sqrt{\lambda_B \rho_B c_{p,B}}$ than the ceramic used in case [SON_CONE_35_4]. Therefore, the transient heat transfer from the sample to the insulator is retarded, which favours the temperature rise at the backface and in the whole sample thickness, and, in turn, accelerates the degradation.

These three experimental cases allow proposing an estimate of the experimental uncertainty on the proposed quantitative indicators, namely $\approx 20\%$ for the time to peak mass loss rate $t_{\text{peak},1}$, $\approx 30\%$ for the mass loss characteristic times t_{25} , t_{50} and t_{75} , and $\approx 15\%$ for the characteristic times of backface degradation.

5.3. Comparison with numerical results

5.3.1. Characteristic times

The characteristic times obtained in the corresponding numerical simulations are reported in Table 4. Compared to Girardin's experiments, the mass loss characteristic times t_{25} , t_{50} and t_{75} are underestimated by 2%, 16% and 36% for case [GIR_CONE_35_3], which is less than the experimental uncertainty, and by more than 50% for case [GIR_CAMLC_50_3]. In spite of these differences, the backface temperatures are in good agreement at least up to the

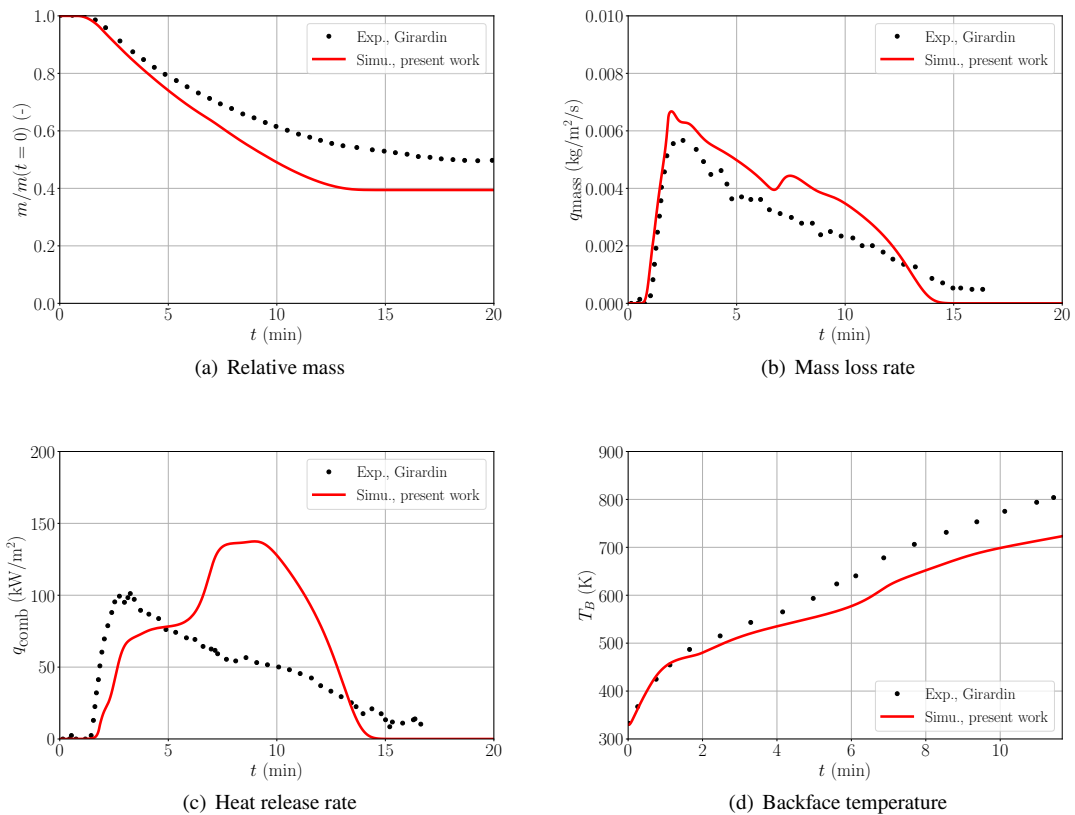
Table 4

Pyrolysis characteristic times (min) obtained in the numerical simulations.

Case	$t_{\text{peak},1}$	$t_{\text{peak},2}$	t_{25}	t_{50}	t_{75}	t_{ATH}	t_{VA}	t_{EVA}
[GIR_CAMLC_50_3]	1.48	(-)	2.71	5.36	8.51	5.13	7.15	14.26
[GIR_CONE_35_3]	1.98	(-)	3.30	5.73	8.71	6.08	7.92	13.23
[SON_CONE_35_4]	2.03	9.12	3.80	6.88	10.81	7.85	10.20	16.93

EVA deacetylation (less than 20% on t_{ATH} and t_{VA} in both cases). The computed mass loss rate is in better agreement for case [SON_CONE_35_4], with 2%, 6% and 14% relative discrepancy on t_{25} , t_{50} and t_{75} .

5.3.2. Detailed analysis of the cone calorimeter experiments in oxydative atmosphere


Figure 4: Comparison between the experimental measurements and the numerical simulation for case [GIR_CONE_35_3].

The time evolutions of the mass losses, mass loss rates and backface temperatures for case [GIR_CONE_35_3], and of the mass losses, mass loss rates and heat release rates for case [SON_CONE_35_4] are reported in Figures 4 and 5. The overestimation of the mass loss rate in spite of a good reproduction of the backface temperature for case

[GIR_CONE_35_3], and the good agreement in terms of mass loss rate for case [SON_CONE_35_4] are confirmed. However, a noticeable difference arises between the computed and experimentally measured heat release rates: in the experimental cases, the heat release rate evolution follows the mass loss rate evolution; in particular, the first peak of mass loss rate is associated with a peak of heat release rate. On the contrary, the numerical simulations do not reproduce the first HRR peak at all, but rather exhibit a delayed peak occurring just before the final extinction and the pyrolysis end. Yet, the analysis of the backface temperature of case [GIR_CONE_35_3] suggests that most of the water vapour should be released before $t_{ATH} = 4.76$ min (experimental) or $t_{ATH} = 6$ min (simulation). This observation is consistent with the computed HRR: before this instant, water vapour is expected to be dominant in the ejected pyrolysis gases and the concentration of produced flammable species is probably negligible, so that the heat release is low; after this ATH dehydration step, the heat release rate increases because only flammable gases are ejected. However, if this expected mechanism clearly arises in the simulations, it does not seem to occur experimentally. The measured HRR rather suggests that a non-negligible amount of flammable gases is released during the first HRR peak and more generally in the first step of the pyrolysis process occurring before t_{ATH} , i.e. during most of the ATH dehydration. Conversely, water vapour seemingly keeps on being released after t_{ATH} , i.e. during most of the EVA decomposition, so that the heat release rate is lower than it would be if only flammable gases were produced. The analysis of the gases released during the pyrolysis process in case [GIR_CAMLC_50_3] in section 5.3.3 will suggest reasons for this inconsistency.

5.3.3. Detailed analysis of test case [GIR_CAMLC_50_3] in inert atmosphere

The material degradation can be further analysed by considering additional gas concentration measurements carried out by Girardin et al., 2015 in the [GIR_CAMLC_50_3] gasification test case. The computed mass loss rate and backface temperature are reported in Figure 6 along with their experimental counterparts. The partial mass loss rates associated with the ATH dehydration and EVA deacetylation and decomposition are also reported in Figure 7.

It must first be noticed that the experimental data confirm the previous observation on the progressive release of water vapour. Indeed, the backface temperature recording (Figure 6.(b)) suggests that the ATH dehydration is supposed to be achieved no later than ≈ 5 min (≈ 7 min if the water vapour production related to the catalytic conversion of the acetic acid to acetone is accounted for as in the present model, see table 4). Nevertheless, Fig. 17 of (Girardin et al., 2015) shows that water vapour keeps on being released until the end of the pyrolysis process, and not only before t_{ATH} as expected according to the present modelling.

Conversely, the numerical results exhibit seemingly successive and separated pyrolysis steps. The in-depth profiles of temperature and reaction rates associated with the four degradation steps of the present model, depicted at times $t \in 1, 3, 5, 7$ min in Figures 8-11, provide more information on the material degradation. At $t \approx 1$ min, the first MLR peak occurs. The whole intumescence has already taken place (the sample surface is at $x = 1.2$ mm relative to its initial

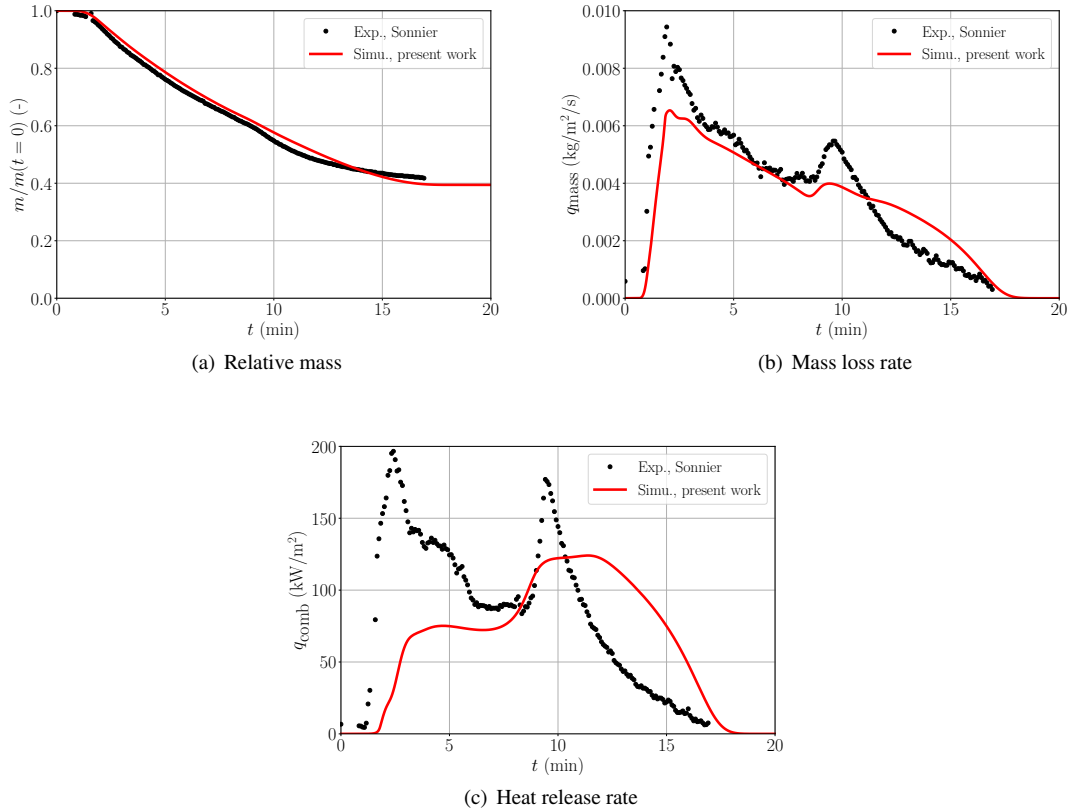


Figure 5: Comparison between the experimental measurements and the numerical simulation for case [SON_CONE_35_4].

position), and the pyrolysis front \mathcal{R}_2 associated with the ATH dehydration starts traveling from the irradiated side to the backside (Figure 8.(b)). At $t = 3$ min, the MLR decreases, the endothermic ATH dehydration hinders the temperature increase inside the material and thus the acceleration of the material degradation. The pyrolysis front associated with the EVA deacetylation \mathcal{R}_3 lags just behind but is clearly separated. This delay between ATH dehydration and EVA deacetylation is also clearly observed in the partial mass loss rates depicted in Figure 7. The last front \mathcal{R}_4 associated with the EVA degradation just appears at the sample surface; hence, the final alumina residual is already present at the sample surface (Figure 9.(b)). The conjunction of the ATH dehydration and of the appearance of the reflective residual may explain the early MLR peak, its rapid decrease and the rapid decrease of the production of water vapour observed in Figure 7. At $t = 5$ min, the ATH dehydration is almost completed in the whole material, so the associated endothermic effect stops. The two pyrolysis zones associated with the EVA deacetylation and final decomposition spread over a large part of the sample thickness; in particular the second reaction explains the rise of the production of hydrocarbons. After $t = 7$ min, the EVA deacetylation is almost completed and only the final step of EVA degradation still takes place in the material.

Such a behaviour, noticeably different from the experimental data, has also been observed in simulations performed by Girardin et al., 2015 with a in-house pyrolysis model. Similarly with the present model, Girardin's model considers the 1D conservation of the solid mass, mass of pyrolysis volatiles and enthalpy conservation. The main difference is in the modelling of the gas transfers. While we apply Fick's law to describe the species diffusion relative to the barycentric mean flow described by Darcy's law, Girardin directly applies Fick's law for the mean flow, regarded as a diffusive process. The results of his simulations (labelled "R.D." for "rapid diffusion" in Figure 6) are similar to those of the present ones. Note that a formal correspondance can be established between the two formulations and between the effective mass diffusion coefficient and the permeability K .

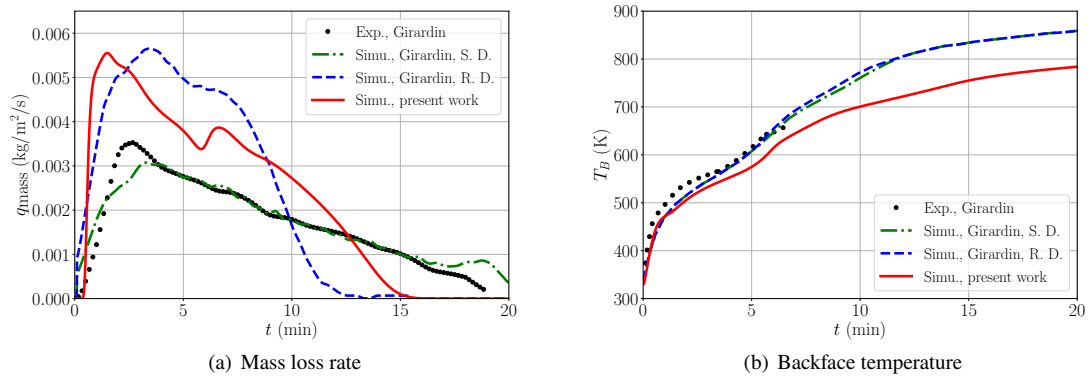


Figure 6: Comparison between the experimental measurements recorded for case [GIR_CAMLC_50_3], the numerical simulations of Girardin et al., 2015 and the present numerical simulation.

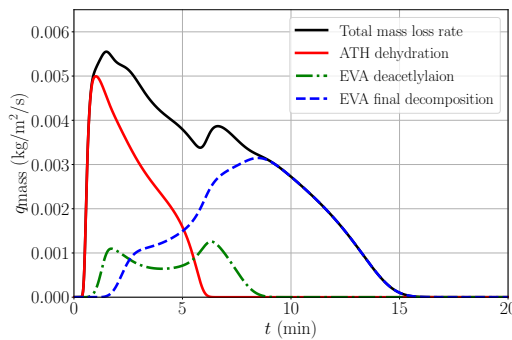


Figure 7: Mass loss rate simulated for case [GIR_CAMLC_50_3], decomposed into gases produced during the ATD dehydration, the EVA deacetylation and the EVA decomposition.

In summary, whereas the thermal response of numerical model is satisfactory (agreement on the backface temperatures), a direct correspondance between the degradation steps observed in thermogravimetric analyses (and

used here through the Arrhenius laws) and the actual degradation steps observed during cone calorimeter experiments does not seem to apply: the ATH dehydration is apparently not yet completed when the whole material is at a temperature larger than required for this reaction. Several possible reasons can explain the shortcoming of the current pyrolysis modelling.

A first reason, raised by Girardin et al., 2015, could be the trapping of a noticeable amount of pyrolysis gases inside the material. Along with the default "rapid diffusion" simulation, a second one ("Slow diffusion") with a considerably decreased value of the gas diffusion ($\approx 10^{-9}$ m²/s against $\approx 10^{-5}$ m²/s), allowed recovering the correct mass loss rate without modifying the backface temperature evolution (data labelled "S.D." for "slow diffusion" in Fig. 6). However, the "rapid diffusion" and the "slow diffusion" models correspond in terms of a Darcy formulation to permeabilities $K = 10^{-14}$ m² and $K = 10^{-18}$ m², respectively, and would result in pressure increases within the material of ≈ 1 atm and $\approx 10^4$ atm, respectively. It is not surprising that such a large pressure is required to delay the gas emission sufficiently to reconcile the measured and predicted MLR curves. The mass of gas to be stored in the medium is a significant fraction of the whole sample mass, and has to be under very high pressure to fit in the pore space. However, this is physically unrealistic in view of very low resistance of the material in its early (glass transition of EVA) and late (weak cohesivity of the alumina grain residual) stages of pyrolysis. Even pressures of the order of 1 atm are hardly conceivable, for the same reasons. Conversely, values $K = 10^{-11}$ m² or $K = 10^{-13}$ m² in the present model originate from a direct modelling based on morphological information and since Darcy's equation is actually solved the pressure increase is known from the simulations and is seen to remain much smaller than 1 atm. As a consequence, the possibility of an important trapping of pyrolysis gases in the material by pressure effects is unlikely.

A second cause for the observed discrepancies deals with the sources of water vapour release. According to the degradation scheme depicted in section 3.1, the ATH dehydration is not the only chemical mechanism responsible for water vapour production; the catalytic conversion of acetic acid to acetone also leads to the production of H₂O along with CO₂. However, considering the low fraction of vinylacetate in the EVA, and assuming a total conversion of acetic acid to acetone, the mass yield of water vapour associated with this mechanism cannot represent more than 1.1% of the total mass of the material (1.0% in the present case considering the acetone yield measured by Girardin et al., 2015) compared to the total 20.8% mass yield associated with the ATH dehydration.

Therefore, the inconsistency between the measured simulated and MLRs and HRRs in cases [GIR_CONE_35_3] and [SON_CONE_35_4] (section 5.3.2), and between the TGA induced kinetic model for ATH and the observed release of water vapour in cone calorimeter in case [GIR_CAMLC_50_3] in the present section, lead to question the relevance of the model for the kinetic dehydration of ATH itself. Indeed, the experimental results obtained in cone calorimeter suggest that the ATH dehydration may be incomplete at the main identified TGA peak near 580 K. In this respect, separate characterizations of ATH (Redaoui et al., 2016; Zivkovic and Dobovisek, 1977; Strekopytov and

Exley, 2006) show that a noticeable amount (between 15% to 20%) of the ATH water content is released between 650 K (end of the peak) and 850 K. Thus, the account of a delayed ATH dehydration could be considered for a better prediction of the material pyrolysis.

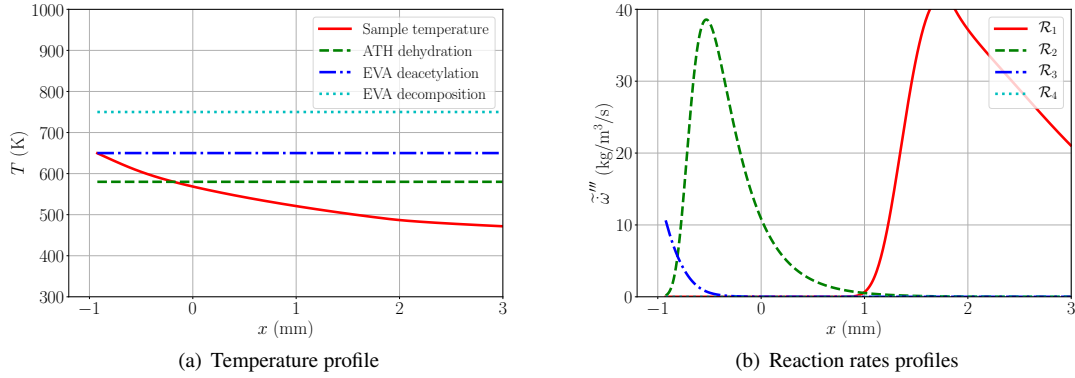


Figure 8: Temperature and reaction rate profiles at $t = 1$ min along the material depth computed for case [GIR_CAMLC_50_3]. The origin $x = 0$ corresponds to the initial sample surface position, before intumescence.

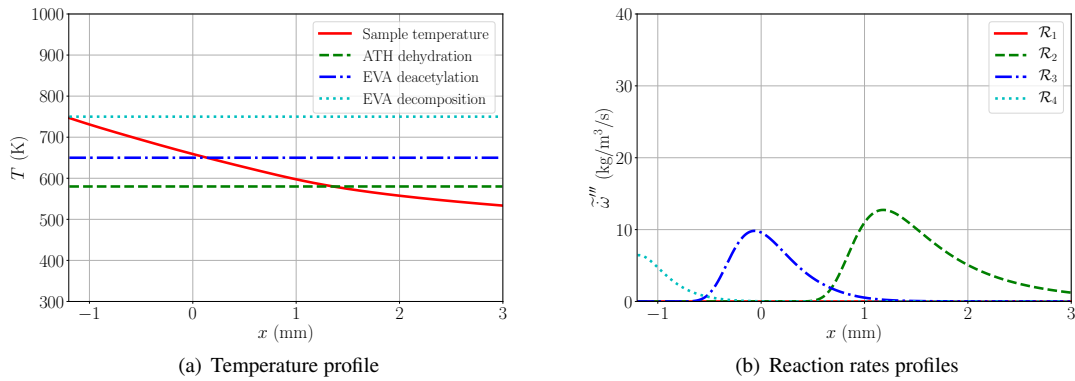


Figure 9: Temperature and reaction rate profiles at $t = 3$ min along the material depth computed for case [GIR_CAMLC_50_3]. The origin $x = 0$ corresponds to the initial sample surface position, before intumescence.

5.4. Global thermal balance analysis

Accounting for boundary conditions (14) and (19), a global enthalpic balance can be derived by integrating the sensible enthalpy conservation equation (12) over the evolving domain that follows the sample volume variations. The global balance reads:

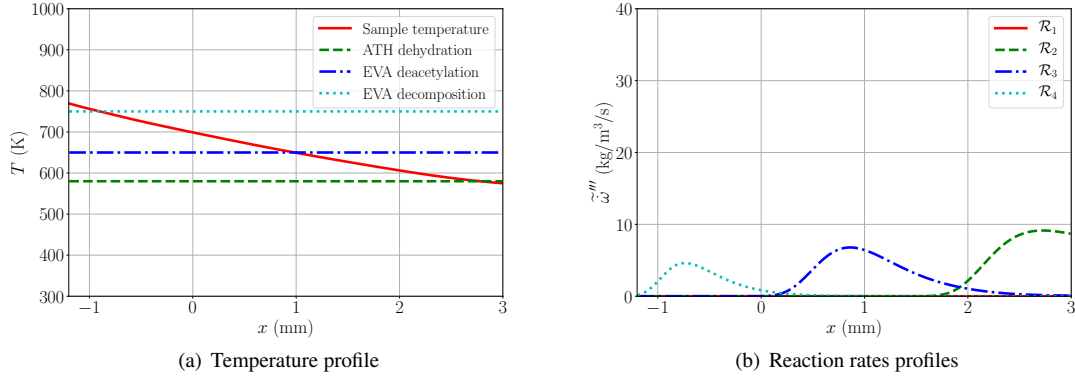


Figure 10: Temperature and reaction rate profiles at $t = 5$ min along the material depth computed for case [GIR_CAMLC_50_3]. The origin $x = 0$ corresponds to the initial sample surface position, before intumescence.

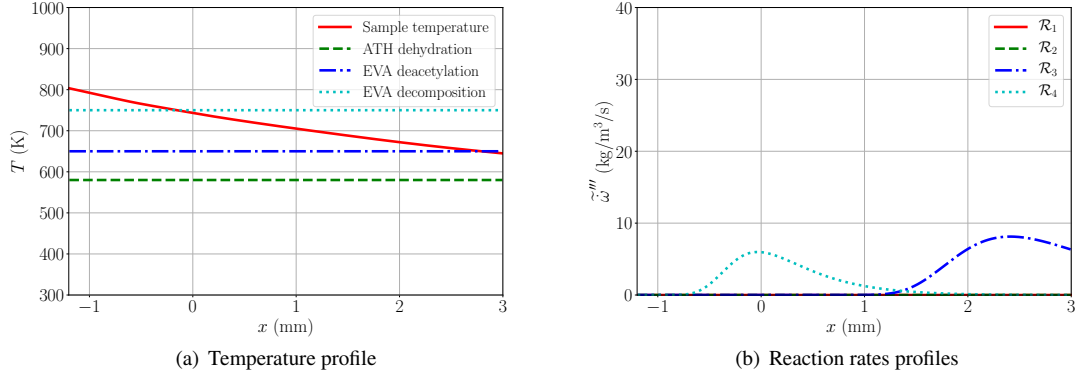


Figure 11: Temperature and reaction rate profiles at $t = 7$ min along the material depth computed for case [GIR_CAMLC_50_3]. The origin $x = 0$ corresponds to the initial sample surface position, before intumescence.

$$\underbrace{\int_0^{\delta_M} \partial_t \left(\sum_{m=1}^{N_M} \widetilde{\rho_{M_m}} \overline{h_{M_m}^s} \right) dx}_{P_{acc,M}} + \underbrace{\int_0^{\delta_M} \partial_t (\phi \overline{\rho_G} \overline{h_G^s}) dx}_{P_{acc,G}} + \underbrace{\int_0^{\delta_M} (\partial_t \overline{p_G} + \overline{u_G} \partial_x \overline{p_G}) dx}_{P_{pwk}} + \underbrace{\int_0^{\delta_M} \sum_{i=1}^{N_R} \Delta h_{R_i} \widetilde{\omega}_i dx}_{\sum_i P_{R_i}} = \underbrace{\left(\phi \overline{\rho_G} \overline{h_G^s} (\overline{u_G} - \overline{u_M}) - \lambda_{eff} \partial_x \overline{T} + \widetilde{q_{rad}} \right)_{MF}}_{q_{MF}} + \underbrace{\left(-\phi \overline{\rho_G} \overline{h_G^s} (\overline{u_G} - \overline{u_M}) + \lambda_{eff} \partial_x \overline{T} - \widetilde{q_{rad}} \right)_{MB}}_{q_{MB}} \quad (25)$$

The integrated terms $P_{acc,M}$, $P_{acc,G}$, P_{pwk} and P_{R_i} correspond to the heat accumulation in the condensed phase and in the gas phase, the pressure work and the heat loss rate associated with the pyrolysis reactions.

At the irradiated face, the total heat flux q_{MF} can be decomposed into the convective heat exchange $q_{\text{exch},MF}$ using Equation (14), the enthalpic flux due to the pyrolysis gases ejection $q_{\text{ej},MF}$ and the net incident radiative flux $q_{\text{rad},MF}$:

$$q_{MF} = \underbrace{h_{\text{exch},MF}(T_F - \bar{T}_{MF})}_{q_{\text{exch},MF}} + \underbrace{\phi \bar{\rho}_G \bar{h}_G^s (\bar{u}_G - \bar{u}_M)}_{q_{\text{ej},MF}} + \underbrace{\widetilde{q}_{\text{rad}}}_{q_{\text{rad},MF}} \quad (26)$$

In turn, according to boundary condition (15), the net incident radiative flux is decomposed as:

$$q_{\text{rad},MF} = q_{\text{rad,inc},MF} + q_{\text{rad,ref},MF} + q_{\text{rad,em},MF} \quad (27)$$

where $q_{\text{rad,inc},MF}$ is the incident part, $q_{\text{rad,ref},MF} = -(1 - \epsilon_{\text{eff}})q_{\text{rad,inc},MF}$ is the reflected part and $q_{\text{rad,em},MF} = -\epsilon_{\text{eff}}\sigma\bar{T}_{MF}^4$ is the emitted part. At the backface, according to boundary condition (19), the heat flux q_{MB} reduces to the conductive part, so that

$$q_{MB} = \lambda_B \partial_x T_B \quad (28)$$

All these volume terms P_{\dagger} and surface heat fluxes q_{\dagger} in Eqns. (26-28) can be compared to the cone heater flux q_{imp} to identify the dominant mechanisms in the heat transfer in the material during its degradation. The following time integrals can also be used to quantify the fraction of incident energy associated with each contribution :

$$H_{\bullet} = \int_0^{t_{\text{end}}} \frac{P_{\bullet}}{q_{\text{imp}}} dt, \quad (29)$$

where $\bullet \in \{\text{acc}, M; \text{acc}, G; \text{pwk}; \mathcal{R}_i\}$ and

$$h_{\bullet} = \int_0^{t_{\text{end}}} \frac{q_{\bullet}}{q_{\text{imp}}} dt, \quad (30)$$

where $\bullet \in \{\text{comb}; \text{rad,inc}, MF; \text{rad,ref}, MF; \text{rad,em}, MF; \text{rad,net}, MF; \text{ech}, MF; \text{ej}, MF; MB\}$ and t_{end} is the time when the mass loss has reached 99.9% of its final value.

The different surface and volume terms of the enthalpy balance associated with the numerical solution obtained for case [GIR_CAMLC_50_3] are reported in Figures 12 and 13. Regarding the radiative balance, the net radiative flux contributing to the material heating rapidly decreases (within 3 min) to less than 50 % of the heat flux imposed by the cone heater, and even less than 30 % after ≈ 8 min, i.e. during a large part of the final EVA decomposition (Figure 12.(b)). This results from the surface emission, which stabilizes at ≈ 30 % of the incident flux after 2 min, but also from the unusually large surface reflexion that converges to ≈ 35 % after 4 min. This particular phenomenon

is specific to EVA-ATH materials whose alumina residuals have a much larger surface reflectivity (here close to 0.4 in the final stages of the material degradation) than other charring polymers. Considering the large uncertainties for the final state material emissivity (effect of the porous structure, spectral behaviour), the correct characterisation of this physical parameter is of great importance for the correct prediction of the material degradation, and its wrong evaluation may contribute to the anomalies observed in section 5.3.3. Compared to these radiative terms, the surface heat losses by convective exchange (term $q_{\text{exch},MF}$) and gas ejection (term $q_{\text{ej},MF}$) contribute in a smaller respect (less than 10 %) and have therefore a weaker influence on the irradiated surface heat balance. In these conditions, the net flux used for the material pyrolysis only represents 32% of the imposed flux after 3 min and 15 % after 7 min.

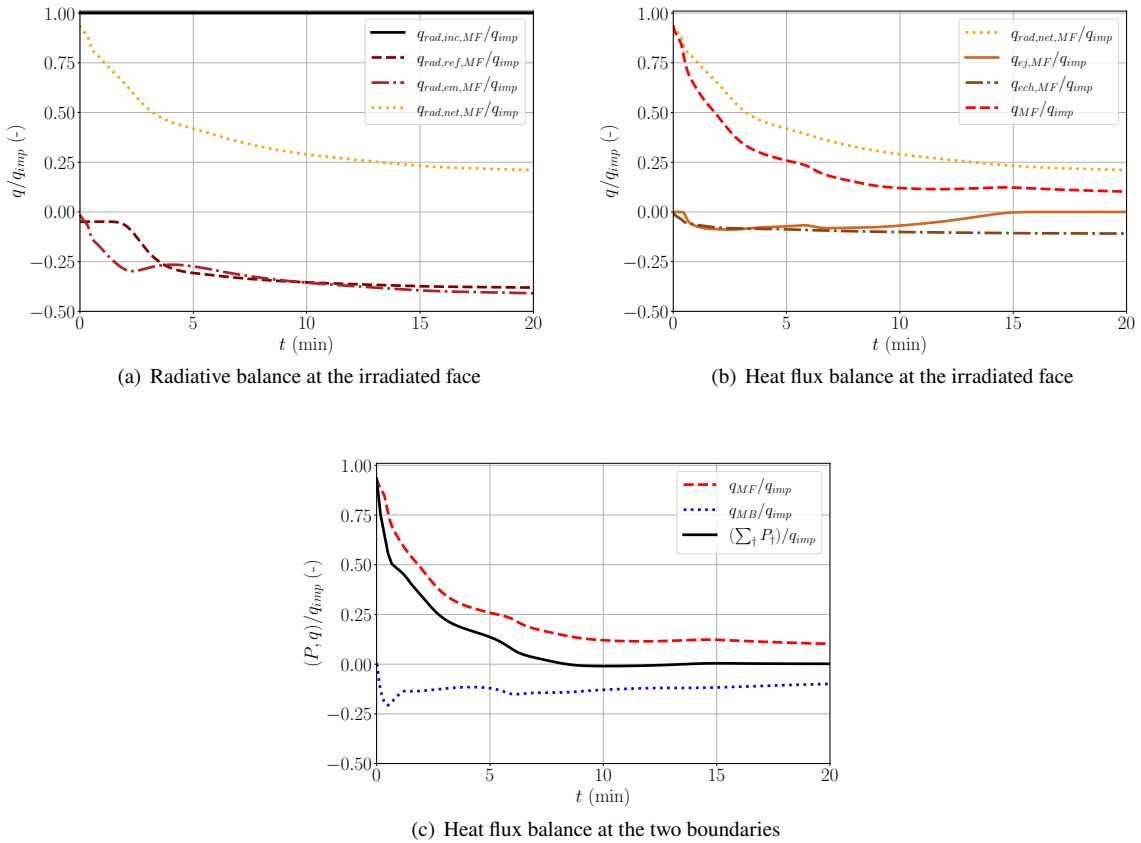


Figure 12: Time evolution of the ratios between the surface terms of the enthalpy balance and the heat flux imposed by the cone heater.

By comparison, the heat lost through the backface insulator (term q_{MB}) represents $\approx 10\%$ of the imposed flux all along the material decomposition except during an initial 1 min transient, and after 7 min it is very close to the net heat flux entering the irradiated side; the volume terms are much smaller than the surface terms, and most of the energy provided at the exposed surface is transferred to the backface. As a consequence, these backface heat losses mostly

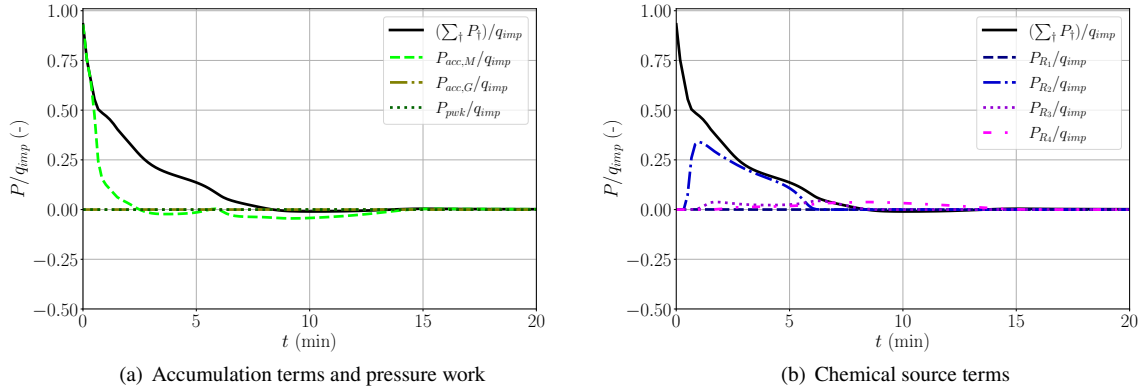


Figure 13: Time evolution of the ratios between the volume terms of the enthalpy balance and the heat flux imposed by the cone heater.

determine the material temperature during this second step of the pyrolysis (EVA degradation). They are therefore a second term that should be modelled with particular care. Note that these orders of magnitude are similar to those associated with their time-integrated counterparts as depicted in Table 5: overall, only 40.5 % of the total cone heat is absorbed by the material, nearly a half of this value ($h_{ej,MF} + h_{exch,MF} = 15.2$ %) is lost by the material because of the convection of the pyrolytic gases and the heat exchange with the surrounding atmosphere, and a similar fraction (13.1 %) is lost at the backface. The net balance $h_{MF} - h_{MB}$ which actually remains in the material, causing its temperature rise and sustaining the pyrolysis, amounts only for 12.1% of q_{imp} .

In the volume terms balance, only four terms exhibit a non-negligible magnitude (sensible enthalpy accumulation $P_{acc,M}$ in the solid phase, and reactive terms P_{R_2} , P_{R_3} and P_{R_4}). Among them, the sensible enthalpy accumulation related to the increase of the material temperature mostly occurs in the early phase of the material degradation, even before the beginning of the ATH dehydration ($t < 1$ min). It corresponds to less than 15 % of the total volume term. Then, overall, the sink terms associated with the endothermic pyrolysis processes correspond to less than a fourth ($\sum_i H_{R_i} = 10.4$ %) of the net incident radiative flux. Specifically, the chemical term associated with the ATH dehydration is dominant between 1 and 5 min and corresponds to ≈ 59 % of the volume terms. The terms associated with the EVA deacetylation H_{R_3} and final decomposition H_{R_4} amount to similar parts, less than 27 % each of the total volume enthalpy balance. Therefore, the volume sink term associated with the ATH dehydration is the third most influential term in this enthalpy balance, and uncertainties on this term may have an influence on the progress of the pyrolysis front inside the material, and consequently on the global material decomposition rate. This observation emphasizes the need for a correct description of the kinetics of the ATH decomposition suggested in section 5.3.3.

Table 5

Surface enthalpy balance: net energy gained or lost by the material at the boundaries, expressed in terms of the ratio with the total energy provided by the cone heater.

h_{comb}	$h_{\text{rad,ref,MF}}$	$h_{\text{rad,em,MF}}$	$h_{\text{rad,net,MF}}$	$h_{\text{ej,MF}}$	$h_{\text{ech,MF}}$	h_{MF}	h_{MB}
129.5%	-30.9%	-28.2%	40.8%	-6.2%	-9.1%	25.5%	-13.3%

An important aspect has not been considered in this analysis of the global energy balance, namely the release of chemical potential energy that would result from the combustion of the pyrolysis gases. From the point of view of a fire, this source term should be compared to the net sink term, namely the net heat flux entering the degrading material. In the present case, during the duration $t_{\text{end}} \approx 15$ min of the complete degradation of the cable sheath material, this sink amounts to $h_{MF} \approx 10.8$ MJ/m². But conversely, the material releases combustible gases for a total amount of chemical potential energy ≈ 62 MJ/m². This occurs predominantly over a time interval from about 3 to 15 min from the onset of the process, as shown in Figure 14. The overall source term exceeds the sink by a factor almost 6. Of course, this should be taken only as an approximation, and it is associated with the particular scenario for the simulation. For instance, part of the energy released when the gases burn radiates back to the material surface, and part of this irradiation contributes to h_{MF} and to the sink term. This is not accounted for in the present simulation under an inert atmosphere. Nevertheless, this would not change the order of magnitude of the source/sink ratio, which shows that the material degradation vigorously contributes to sustain the fire.

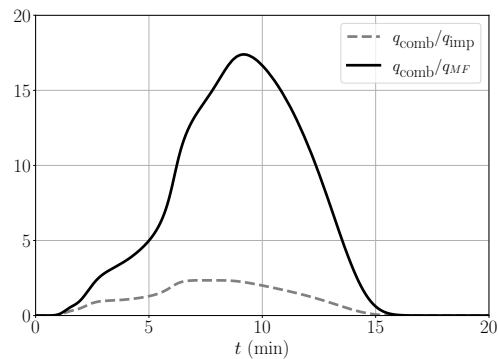


Figure 14: Theoretical heat release rate associated with the flammable gases release: ratio with the cone heater flux and the net flux through the sample surface.

6. Concluding remarks

The model used in the present work to simulate the pyrolysis of EVA-ATH compounds, including a detailed degradation scheme and an original description of the material effective conductivity and final state surface emissivity,

Table 6

Volume enthalpy balance: internal terms of the enthalpy conservation equation expressed in terms of a ratio with the total energy provided by the cone heater

$\sum_{\dagger} H_{\dagger}$	$H_{acc,M}$	$H_{acc,G}$	H_{pwk}	H_{R_1}	H_{R_2}	H_{R_3}	H_{R_4}
12.2 %	1.5 %	< 0.1 %	< 0.1 %	< 0.1 %	7.2 %	1.4 %	1.9 %

yields results similar to those of simulations of the literature carried out with equivalent material properties (Girardin et al., 2015), but some noticeable discrepancies with the experimental data. Typically, the predicted abrupt ending of the process is classical and stems from simplifying hypotheses such as the neglected side effects in cone calorimeter experiments or an oversimplified chemical model with single reactions to represent a more complex reality. However, other differences such as the overestimation of the mass loss rate compared to gasification experiments and the emission of water vapour at times when the observed and predicted backface temperature are larger than the ATH dehydration temperature, have already been observed in the literature (Girardin et al., 2015; Witkowski et al., 2015) but are specific to the EVA-ATH compounds. In the past, these differences have been interpreted in terms of accumulation of pyrolysis gases, especially water vapour, in the pores appearing in the intermediate states of the degrading material, tentatively accounted for by the tuning of some transport coefficients in order to predict the correct mass loss rate. However, these modified coefficients, related to the permeability in our formalism, imply values of the gas pressure that indeed allow thereby to store a large amount of gas in the material and delay its emission, but that are totally unrealistic considering that the gas is embedded in a liquefied matrix. Furthermore, the comparison between cone calorimeter experiments in usual atmospheric conditions (Girardin, 2016; Sonnier et al., 2016) and the present numerical simulations suggests that noticeable values of the HRR occur at times when water vapour should be dominant among the pyrolysis gases, and thus that the global release of the different gaseous species is not correctly predicted by the usual sequencing of chemical mechanisms.

In this respect, several enhancements related to the degradation scheme can be considered. In the present work, the EVA deacetylation has been considered separately from the ATH dehydration and the partial catalytic conversion of acetic acid to acetone has been included. This could explain the release of water vapour after the ATH dehydration and of flammable gases before the main step of EVA decomposition, but the low value of the VA content in EVA (28%) precludes a noticeable effect of this separated reaction. There is also evidence that ATH dehydration actually involves two steps, with two thirds of the water released according to a kinetic law corresponding to that implemented in the present model, but up to a remaining third at a much higher temperature, overlapping the range for the final EVA degradation (Zivkovic and Dobovisek, 1977; Rivas Mercury et al., 2006; Zhu et al., 2010). This feature will be

implemented in the near future, and the model sensitivity to a delayed release of water vapour in the chemical scheme will be studied.

More generally, the large number of physical parameters involved in the pyrolysis of EVA-ATH compounds requires a thorough investigation of the sensitivity of the present model to their related uncertainties, that can easily be carried out considering the full parametrization of the effective material properties from the properties of the constituents. The present work suggests some (non-exhaustive) such examples of sensitivity analyses. Correlatively with the previous observations on the uncertainties on the degradation path, the effect of different values of the ATH content and the VA content in EVA should be studied, as well as the uncertain parameters related to the material degradation previously evoked. The thermal balance depicted in the present work also suggests that boundary parameters such as the emissivity of the material residual and the parameters related to the backface condition play a major role in the heat transfer in the material and therefore the global kinetics of its degradation. Finally, the parametrization of the conceptual models for several effective properties (conductivity, surface emissivity/transmissivity) proposed in earlier works (Shi, 2019; Shi et al., 2020) is perfectly suited to study the effect of modifications or uncertainties on the associated physical properties of the constituents and the characteristic features of the morphology of the material residuals (pore distribution and aspect ratio, material intumescence, conductivity and emissivity of the constituents, etc.).

Declaration of Competing Interest

The authors declare that they have no known competing financial interests or personal relationships that could have appeared to influence the work reported in this paper.

Acknowledgements

This work pertains to the French government program "Investissements d'Avenir" (LABEX INTERACTIFS, reference ANR-11-LABX-0017-01)

A. Detail of the material physical properties

The mass stoichiometric coefficients for degradation scheme (3) and the Arrhenius laws coefficients for the reaction rates (22) are depicted in Tables 7 and 8.

For the enthalpy laws, the coefficients of the expression $c_p = a + bT - c/T^2$ for the specific heats of the pseudo-materials are given in Table 9. The heats of combustion of the flammable gaseous species are: $\Delta h_{c,3} = 14.0 \times 10^6$ J/kg, $\Delta h_{c,4} = 27.9 \times 10^6$ J/kg, $\Delta h_{c,5} = 49.6 \times 10^6$ J/kg, $\Delta h_{c,6} = 43.7 \times 10^6$ J/kg, $\Delta h_{c,7} = 41.5 \times 10^6$ J/kg and $\Delta h_{c,8} = 27.6 \times 10^6$ J/kg.

Table 7

Condensed pseudo-materials and gas stoichiometric coefficients associated with the degradation reactions of the 4-step EVA-ATH degradation path.

Reaction	μ_i	ν_{ik}
\mathcal{R}_1	$1 - \nu_{11}$	$\nu_{11} = 1.06 \times 10^{-4}$
\mathcal{R}_2	0.792	$\nu_{21} = 0.208$
\mathcal{R}_3	0.901	$\nu_{31} = 0.013, \nu_{32} = 0.032$ $\nu_{33} = 0.012, \nu_{34} = 0.042$
\mathcal{R}_4	0.552	$\nu_{45} = 0.047, \nu_{46} = 0.129$ $\nu_{47} = 0.073, \nu_{48} = 0.199$

Table 8

Arrhenius constants and heats of pyrolysis associated with the degradation reactions of the 4-step EVA-ATH degradation path.

Reaction	$A_{S,i}$ (s^{-1})	$E_{a,i}$ (kJ/mol)	$\Delta h_{p,i}$ (kJ/kg)
\mathcal{R}_1	1.70×10^{16}	162	0.364
\mathcal{R}_2	8.72×10^{12}	162	710
\mathcal{R}_3	4.23×10^{12}	180	172
\mathcal{R}_4	1.23×10^{17}	268	268

Table 9

Specific heat coefficients for ATH (Wefers and Misra, 1987), alumina (Auerkari, 1996) and EVA (Stoliarov et al., 2009a).

	a (J/kg/K)	b (J/kg/K ²)	c (J K /kg)
ATH	646.92	2.301	1.405×10^7
alumina	1044.6	0.1742	2.796×10^7
EVA	51.614	4.3946	0

The temperature dependences of the EVA and alumina conductivities are taken from Girardin, 2016 and Powell et al., 1966, respectively; for ATH, the conductivity is extracted from the value given by Horai, 1971, corrected to account for the effects of the measurement setup and the tested alumina porosity, as depicted in App. A5 of (Shi, 2019), and the temperature dependence is set to the typical $1/T$ decay for minerals (Roufousse and Klemens, 1974); finally, the gas phase conductivity (steam and pyrolysis gases) are taken from (McBride et al., 1993). These temperature dependences are depicted in figure 15.

B. Time step and grid convergence

The grid convergence studied in terms of temporal evolution of mass loss rate by Shi (2019) is further analysed in the present work. Case [GIR_CONE_35_3] is considered as an example. Simulations with separate variations on the initial grid cell size $\delta x \in \{5 \times 10^{-6}, 1 \times 10^{-5}, 2 \times 10^{-5}, 4 \times 10^{-5}, 8 \times 10^{-5}, 2 \times 10^{-4}\}$ m and the time step

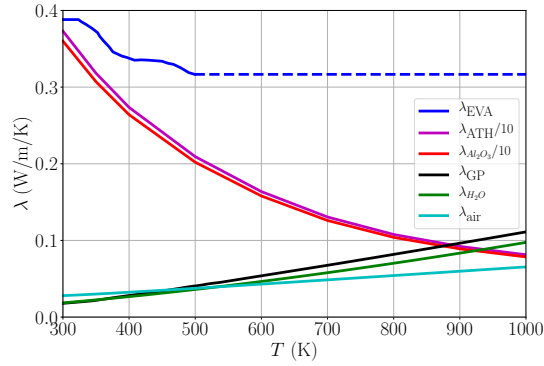


Figure 15: Thermal conductivities of the constituents as functions of the temperature.

$\delta t \in \{0.01, 0.1, 1\}$ s are carried out. The grid and time step convergences are assessed by evaluating the relative error $(t_c - t_{c,\infty})/t_{c,\infty}$ on the characteristic times t_c depicted in section 5.3.1, obtained for each simulation; $t_{c,\infty}$ denotes the extrapolated limit of these characteristic times for $\delta x \rightarrow 0$ and $\delta t \rightarrow 0$. These relative errors are reported in Figures 16. For the grid convergence, the maximum error obtained for the grid cell size $\delta x = 2 \times 10^{-5}$ m used in the study is of 2.5% for t_{EVA} , which is acceptable. The grid cell size must be four times smaller to reach less than 1% error according to the first order spatial accuracy. For the time step convergence, the error remains below 1% as soon as $\delta t = 1$ s.

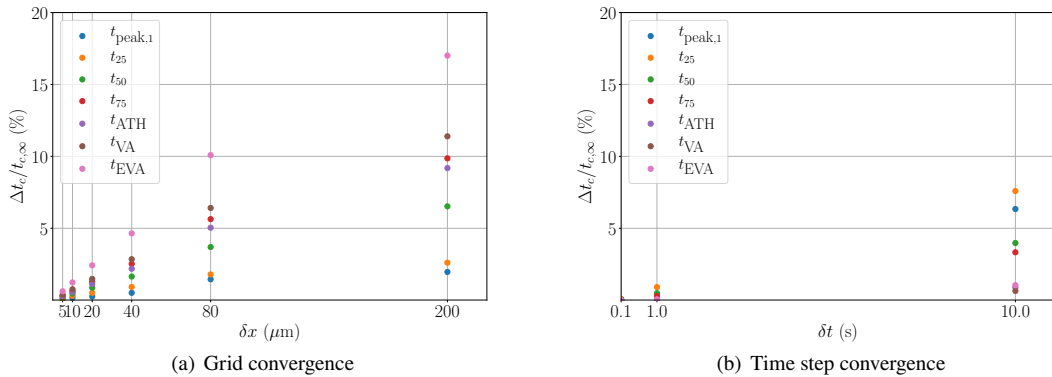


Figure 16: Relative errors on the calculated characteristic times (definition in section 5.3.1) with respect to the values extrapolated for infinite accuracy.

References

- Agarwal, G., Lattimer, B., 2012. Method for measuring the standard heat of decomposition of materials. *Thermochimica Acta* 545, 34–47.
- Auerkari, P., 1996. Mechanical and physical properties of engineering alumina ceramics. Research notes 1792. VTT Manufacturing Technology.
- Babik, F., 2021a. CALIF³S-ISIS V6: Physical modelling. Technical Report IRSN/2021-232. IRSN/PSN-RES/SA2I/LIE.

- Babik, F., 2021b. CALIF³S-ISIS V6: Validation. Technical Report IRSN/2021-232. IRSN/PSN-RES/SA2I/LIE.
- Bal, N., Rein, G., 2015. On the effect of inverse modelling and compensation effects in computational pyrolysis for fire scenarios. *Fire Safety Journal* 72, 68 – 76.
- Bedford, R.E., 1988. Calculation of Effective Emissivities of Cavity Sources of Thermal Radiation. John Wiley & Sons, Ltd. chapter 12. pp. 651–772.
- Bhargava, A., Hees, P.V., Husted, B., Junior, A.R., Neumeister, C., 2019. Performance analysis of a heat transfer and sub-grid chemical reaction distributed activation energy model for fire simulations. *Journal of Fire Sciences* 37, 18–46.
- Boyer, G., 2017. Fully coupled cfd simulation of the pyrolysis of non-charring polymers: A predictive approach. *Fire Safety Journal* 91, 208–217. *Fire Safety Science: Proceedings of the 12th International Symposium*.
- Bruggeman, D.A.G., 1935. Berechnung verschiedener physikalischer konstanten von heterogenen substanzen. i. dielektrizitätskonstanten und leitfähigkeiten der mischkörper aus isotropen substanzen. *Annalen der Physik* 416, 636–664.
- Coelho, A., Costa, L., Marques, M., Fonseca, I., Lemos, A., Lemos, F., 2010. Using simultaneous dsc/tg to analyze the kinetics of polyethylene degradation — catalytic cracking using hy and hzsm-5 zeolites. *Reaction Kinetics, Mechanisms and Catalysis* 99, 5–15.
- Donea, J., Huerta, A., Ponthot, J.P., Rodríguez-Ferran, A., 2004. *Arbitrary Lagrangian Eulerian Methods*. John Wiley & Sons, Ltd.
- Girardin, B., 2016. Numerical modelling and small scale testing of fire performances for halogen-free cable. Ph.D. thesis. Université Lille1 - Sciences et Technologies. Lille.
- Girardin, B., Fontaine, G., Duquesne, S., Forsth, M., Bourbigot, S., 2015. Characterization of thermo-physical properties of eva/ath: Application to gasification experiments and pyrolysis modeling. *Materials (Basel)* 161, 7837–7863.
- Hemingway, B.S., Robie, R.A., Fisher, J.R., Wilson, W.H., 1977. Heat capacities of gibbsite, Al(OH)₃, between 13 and 480 k and magnesite, MgCO₃, between 13 and 380 k and their standard entropies at 289. 15 k, and the heat capacities of calorimetry conference benzoic acid between 12 and 316 k. *Jour. Research U. S. Geol. Survey* 5, 797,806.
- Hoffendahl, C., Fontaine, G., Duquesne, S., Taschner, F., Mezger, M., Bourbigot, S., 2015. The combination of aluminum trihydroxide (ath) and melamine borate (mb) as fire retardant additives for elastomeric ethylene vinyl acetate (eva). *Polymer Degradation and Stability* 115, 77 – 88.
- Horai, K.i., 1971. Thermal conductivity of rock-forming minerals. *Journal of Geophysical Research (1896-1977)* 76, 1278–1308.
- Kanury, A., 1975. *Introduction to Combustion Phenomena*. Gordon and Breach Science.
- Kumar, S., Singh, R.K., 2013. Thermolysis of high-density polyethylene to petroleum products. *Journal of Petroleum Engineering* 28. 987568.
- Kuo, K.K., 1986. *Principles of Combustion*. John Wiley & Sons, Inc.
- Landauer, R., 1952. The electrical resistance of binary metallic mixtures. *Journal of Applied Physics* 23, 779–784.
- Laoutid, F., Lorgouilloux, M., Bonnaud, L., Lesueur, D., Dubois, P., 2017. Fire retardant behaviour of halogen-free calcium-based hydrated minerals. *Polymer Degradation and Stability* 136, 89 – 97.
- Leventon, I.T., Li, J., Stoliarov, S.I., 2015. A flame spread simulation based on a comprehensive solid pyrolysis model coupled with a detailed empirical flame structure representation. *Combustion and Flame* 162, 3884 – 3895.
- Linstrom, P.J., Mallard, W.G., 2001. The NIST chemistry webbook: A chemical data resource on the internet. *Journal of Chemical & Engineering Data* 46, 1059–1063.
- Marcilla, A., Beltrán, M., 1995. Kinetic study of the thermal decomposition of polystyrene and polyethylene-vinyl acetate graft copolymers by thermogravimetric analysis. *Polymer Degradation and Stability* 50, 117 – 124.
- Matala, A., Hostikka, S., 2011. Pyrolysis modelling of pvc cable materials, in: for *Fire Safety Science*, I.A. (Ed.), *International Symposium of Fire Safety Science*, International Association for Fire Safety Science. pp. 917–930.

- Matala, A., Lautenberger, C., Hostikka, S., 2012. Generalized direct method for pyrolysis kinetic parameter estimation and comparison to existing methods. *Journal of Fire Sciences* 30, 339–356.
- Mc Grattan, K.B., Lock, A., Marsh, N., Nyden, M.R., Price, M., Morgan, A.B., Galaska, M., Schenck, K., 2010. Cable Heat Release, Ignition, and Spread in Tray Installations During Fire (CHRISTIFIRE) - Volume 1: Horizontal Trays. NUREG Report CR-7010, Vol. 1. Office of Nuclear Regulatory Research.
- McBride, B., Gordon, S., Reno, M.A., 1993. Coefficients for calculating thermodynamic and transport properties of individual species. NASA Technical Memorandum 4513 .
- Meinier, R., Sonnier, R., Zavaleta, P., Suard, S., Ferry, L., 2017. Fire behavior of halogen-free flame retardant electrical cables with the cone calorimeter. *Journal of Hazardous Materials* 342, 306–316.
- Modest, M.F., 2003. Radiative Heat Transfer. Second ed., Academic Press - Elsevier.
- Powell, R.W., Liley, P.E., He, J., 1966. Thermal conductivity of selected materials. Washington : U. S. Dept. of Commerce, National Bureau of Standards.
- Redaoui, D., Sahnoune, F., Heraiz, M., Rafhdi, A., 2016. Mechanism and kinetic parameters of the thermal decomposition of gibbsite $\text{al}(\text{oh})_3$ by thermogravimetric analysis. *Acta Physica Polonica A* 131, 362–365. Special Issue of the 6th International Congress & Exhibition (APMAS2016), Maslak, Istanbul, Turkey.
- Rivas Mercury, J.M., Pena, P., H. de Aza, A., 2006. On the decomposition of synthetic gibbsite studied by neutron thermodiffractometr. *J. Am. Ceram. Soc.* 89, 3728–3733.
- Roufousse, M., Klemens, P., 1974. Lattice thermal conductivity of minerals at high temperatures. *Journal of Geophysical Research (1896-1977)* 79, 703–705.
- Rozenbaum, O., De Sousa Meneses, D., Echegut, P., 2009. Texture and porosity effects on the thermal radiative behavior of alumina ceramics. *International Journal of Thermophysics* 30, 580–590.
- Sauerwein, R., 2014. Mineral Filler Flame Retardants. John Wiley & Sons, Ltd. chapter 3. pp. 75–141.
- Shi, J., 2019. Simulation de la pyrolyse de gaines de câbles électriques exposées au feu: Caractérisation et modélisation de la morphologie et de la conductivité thermique selon l'état de dégradation. Ph.D. thesis. Université de Poitiers. Poitiers.
- Shi, J., Boyer, G., Mourzenko, V., Thovert, J.F., 2020. Evolutive models for the geometry and heat conductivity of an intumescent eva-ath composite during its thermal degradation. *Materials* 13, 5258.
- Shi, J., Boyer, G., Thovert, J.F., 2018. Simulation of the pyrolysis of charring polymers: influence of the porous media properties. *Journal of Physics: Conference Series* 1107, 032008.
- Sih, S.S., Barlow, J.W., 2004. The prediction of the emissivity and thermal conductivity of powder beds. *Particulate Science and Technology* 22, 291–304.
- Sonnier, R., Viretto, A., Dumazert, L., Longerey, M., Buonomo, S., Gallard, B., Longuet, C., Cavodeau, F., Lamy, R., Freitag, A., 2016. Fire retardant benefits of combining aluminum hydroxide and silica in ethylene-vinyl acetate copolymer (eva). *Polymer Degradation and Stability* 128, 228 – 236.
- Soudais, Y., Moga, L., Blazek, J., Lemort, F., 2007. Coupled dta-tga-ft-ir investigation of pyrolytic decomposition of eva, pvc and cellulose. *Journal of Analytical and Applied Pyrolysis* 78, 46 – 57.
- Stoliarov, S.I., Crowley, S., Lyon, R.E., Linteris, G.T., 2009a. The effect of variation in polymer properties on the rate of burning. *Fire and Materials* 33, 257–271.

- Stoliarov, S.I., Crowley, S., Walters, R.N., Lyon, R.E., 2010. Prediction of the burning rates of charring polymers. *Combustion and Flame* 157, 2024–2034.
- Stoliarov, S.I., Safronava, S., Lyon, R.E., 2009b. Prediction of the burning rates of non-charring polymers. *Combustion and Flame* 156, 1068–1083.
- Strekopytov, S., Exley, C., 2006. Thermal analyses of aluminium hydroxide and hydroxyaluminosilicates. *Polyhedron* 25, 1707–1713.
- Swann, J.D., Ding, Y., Stoliarov, S.I., 2019. Characterization of pyrolysis and combustion of rigid poly(vinyl chloride) using two-dimensional modeling. *International Journal of Heat and Mass Transfer* 132, 347 – 361.
- Tsilingiris, P., 2003. Comparative evaluation of the infrared transmission of polymer films. *Energy Conversion and Management* 44, 2839–2856.
- Wefers, K., Misra, C., 1987. *Oxides and Hydroxides of Aluminum*. Alcoa Technical Paper 19. Alcoa Laboratories.
- Witkowski, A., 2012. The use of numerical methods to interpret polymer decomposition data. Ph.D. thesis. University of Central Lancashire.
- Witkowski, A., Girardin, B., Försth, M., Hewitt, F., Fontaine, G., Duquesne, S., Bourbigot, S., T., H., 2015. Development of an anaerobic pyrolysis model for fire retardant cable sheathing materials. *Polymer Degradation and Stability* 113, 208–217.
- Witkowski, A., Stec, A.A., Hull, T.R., 2012. The influence of metal hydroxide fire retardants and nanoclay on the thermal decomposition of eva. *Polymer Degradation and Stability* 97, 2231 – 2240.
- Zavaleta, P., Audouin, L., 2017. Cable tray fire tests in a confined and mechanically ventilated facility. *Fire and Materials* 42, 28–43.
- Zavaleta, P., Charbaut, S., Basso, G., Audouin, L., 2013. Multiple horizontal cable tray fire in open atmosphere, in: *Proceedings of the Fire and Materials 2013 Conference*, Interscience Communications Limited, San Francisco. pp. 57–68.
- Zavaleta, P., Suard, S., Audouin, L., 2019. Cable tray fire tests with halogenated electric cables in a confined and mechanically-ventilated facility. *Fire and Materials* 43, 543–560.
- Zhu, B., Fang, B., Li, X., 2010. Dehydration reactions and kinetic parameters of gibbsite. *Ceramics International* 36, 2493 – 2498.
- Zivkovic, Z.D., Dobovisek, B., 1977. Kinetics of aluminium hydroxyde dehydration. *Journal of Thermal Analysis* 12, 207–215.